To Dissociate or Decompose: Investigating gas phase rearrangement of some simple to complex compounds using Mass Spectrometry and Thermal Analysis

By

Calvin A. Austin

Submitted in Partial Fulfillment of the Requirements

for the Degree of

Master of Science

in the

Chemistry

Program

YOUNGSTOWN STATE UNIVERSITY

August 8, 2008

To Dissociate or Decompose: Investigating gas phase rearrangement of some simple to complex compounds using Mass Spectrometry and Thermal Analysis

Calvin A. Austin

Signature: _____

Calvin A. Austin Date

Approvals:

_____

Dr. Brian Leskiw Date
Thesis Advisor

_____

Dr. Peter Norris Date
Committee Member

_____

Dr. Howard Mettee Date
Committee Member

_____

Dr. Peter J. Kasvinsky Date
Dean of School of Graduate Studies & Research

Abstract

Mass Spectrometry and Thermal Analysis were used to investigate the fragmentation/decomposition pathways of some organic compounds. The role the functional group plays in the fragmentation of the molecular ion was investigated by using substituted simple organic molecules along with similarly more complex organic molecules. By working with this array of compounds, it was determine that one fragmentation/decomposition pathway could be favored over another. The thermal stability, melting and boiling points, fragmentation patterns and decomposition pathways were determined for several phenolic analogs to correlate these variables.

Acknowledgements

I want to thank my mother, who has raised me to never give up and to challenge myself. I especially like to thank my research advisor, Dr. Brian Leskiw, who has giving me the guidance and confidence needed to pursue a PhD in Chemistry. I would also like to thank Dr. Peter Norris for 3 year of sound advice and support in every aspect of my career here at YSU. I would like thank my fellow graduates' student for making life very comfortable here in the Chemistry department. I would also like thank Ray, Matt, and Roland for all their help with my project, classes, and the company over the past 2 years. I would like thank Dr. Howard Mettee for reviewing my thesis and providing constructive help towards the completions of my thesis. I would also like to thank Kris for supporting me even when I doubted myself. Lastly, I would like thank the YSU chemistry department for accepting me as a part of the family not just another student.

Table of Contents

List of Figures **Page**

List of Tables **Page**

List of Schemes **Page**

Chapter 1: Introduction

1. Introduction

Mass Spectrometry (MS) and Thermal Analysis (TA) are two physical methods of analysis that are often times used in parallel with each other. The complementary nature of these techniques has been demonstrated for some species where the fragmentation and/or subsequent degradation processes began at a similar location within the molecule, i.e.: the weaker bonds. Mass spectrometry and thermal analysis data has been useful in elucidating some structure components of newly synthesized molecules, but a universal comparison has not been possible.[1] While a variety of processes can occur in mass spectrometry, those processes that are energetically favorable will ultimately dominate and the resulting species will be very evident given its relative ion intensity. In thermal analysis, the molecules are continuously energized and deactivated by gas evolution, where any change in energy is reflected in the change in temperature.[2] Through the analysis of gas phase rearrangements within the mass spectrometer and a careful comparison with thermal analysis, fragmentation and decomposition pathways can be explored.

Mass Spectrometry and Thermal Analysis has been around for some time, but recently there have been many studies published on MS and TA coupled with other physico-chemical methods. MS is an invaluable analytical tool which can also shed light on various physical characteristics such as binding energies and proton affinity within a molecule.[3] Mass spectrometry has been applied to numerous fields and areas of interest including, for example, the analysis of peptides, proteins, and nucleic acids along with applications in medical research and environmental sciences. Molecular weight

determination of an unknown is perhaps the most common application of MS, especially when analyzing organic compounds.[4]

The use of Thermal Gravimetric Analysis (TGA) and Differential Scanning Calorimetry (DSC), two examples of thermal analysis, is very common in the analysis of polymers and pharmaceuticals. These techniques also have applications in quality control, geology, and material science. With DSC, one can obtain calorimetry data that includes heat capacity, heats of reaction, and phase changes. From TGA, one can measure the energy changes associated with processes of decomposition, dehydration, and the oxidation of compounds.[5] It is generally accepted that Thermal Analysis gives information that is impossible to obtain by other methods.[5] This very fact makes the interpretation of Thermal Analysis data sometimes very difficult.

The fragmentation and thermal decomposition mechanisms of a series of phenol analogs were investigated and are described herein. Phenols play an important role in many natural and technical processes.[6] By tailoring the widely investigated phenol molecules and related derivatives, attempts were made to inhibit the fragmentation pathway and/or promote the formation of a new fragment and/or species. Alkyl substituted phenols were studied because they are readily available, form stable fragments, and can host a variety of functional groups. The role specific functional groups play is examined where the simple placement of the substituent is found to influence various gas phase reaction pathways. We later hope to apply these techniques to investigate more complex species, namely natural product carbohydrates. Natural product chemistry involves the synthesis, characterization, and identification of

compounds normally synthesized by a living organism. These types of compounds have proven to have antibiotic capability due to the role carbohydrates play in daily biological functions.

Chapter 2: Background

2.1. Mass Spectrometry and Instruments

2.1.1. Mass Spectrometry

Mass spectrometry is an analytical technique that is often employed to identify unknown compounds. Applications of this technique encompass multiple research disciplines including chemistry, biology, and forensic science. While mass spectrometry (MS) has evolved in complexity over the years, its inherent ability to precisely identify the atomic composition of unknown compounds has obvious importance with a variety of applications. There are several instruments used in this research project and before details of each technique are provided, a brief description of mass spectrometry is given below.

All mass spectrometers can be broken down into three distinct pieces beginning with ionization, followed by the mass analyzers, and finally the detector. The ion source is where samples of interest, either gaseous, liquids, or solids, are ionized. Ionization processes vary, depending on the technique, but can either ionize the species intact or cause fragmentation. Fragmentation is the dissociation leading to fragments that are either neutral, positive, or negatively charge. Following ionization, the mass analyzer discriminates ions based on some mass to charge ratio. The analyzer separates the ions and detection follows. A few different mass spectrometers were used in this study including the GCQ and Esquire, as well as two different thermal analysis techniques.

2.1.2. Finnigan GCQ/CI, EI, Direct Insertion Probe

The first instrument to be discussed is the GCQ. This instrument can ionize samples via chemical (CI) and electron ionization (EI) and utilizes a quadrapole mass analyzer, and an ion trap.[7] While the instrument is capable of chemical ionization, which is a soft method of ionization, electron impact was used exclusively. EI is perhaps the most common ionization technique used in MS with a typical energy of 70 eV. Mass spectrometry can explain reaction mechanisms involved in: proton transfer, charge exchange, electrophilic addition, and anion abstraction to name a few. The GCQ also has the capability to analyze solid samples directly using a direct insertion probe.

Figure 2.1: Finnigan GCQ with Direct-Insertion Probe.

The direct insertion probe capability is a large advantage of the GCQ instrument, where the probe consists of a retractable metal rod that can be inserted into the ion source via a vacuum lock.[8] This approach provides the advantage that it only requires a small amount of sample for analysis, which is due to the low pressure in the ionization area and the proximity of the sample to the ionization source.

2.1.3. Bruker Esquire-LC/ ESI/APCI

The Bruker Esquire-LC is a high performance liquid chromatograph/mass spectrometer system with an advanced electrospray/atmospheric chemical ionization(ESI/APCI) ion source combined with a multipole ion trap.[9]

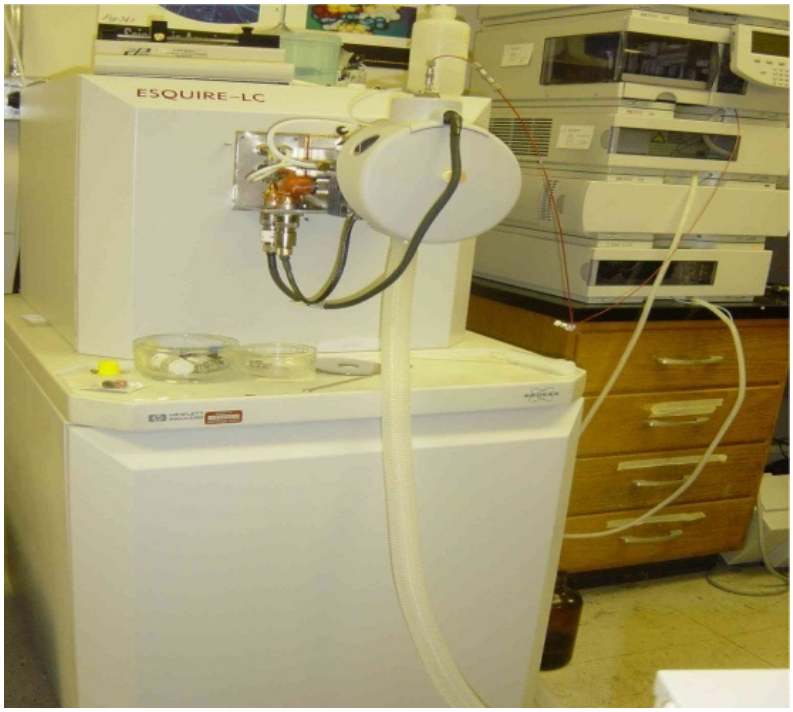

Figure 2.2: Bruker Esquire-LC

This instrument has many capabilities, especially when studying the energetics of those reactions that are taking place inside the instrument. ESI is a soft ionization

technique that limits the fragmentation of the parent molecule. This ionization technique works by applying a strong electric field to a liquid passing through a capillary tube.[3] This field induces a charge accumulation at the liquid surface which then breaks up to form highly charged droplets. As the solvents contained in these droplets evaporate, they shrink to the point where the repelling columbic forces cause their explosion.[3] The resulting ions are analyzed.

APCI uses gas-phase ion-molecule reactions at atmospheric pressure. Ions are formed from a liquid flow introduced into the source region maintained at atmospheric pressure, where the ion source contains sample ions mixed with the solvent vapor and the ambient gas.[10] APCI differs from ESI due to the fact that APCI uses a heater to induce collisions with sample ions, solvent vapors, and the ambient gas.

For both the GCQ and the Esquire mass spectrometers, an Ion Trap is used to collect ions. Trapping is achieved because of the oscillating potential difference established between the ring electrode and end-caps which results in a quadrupolar field. The ions are selected based on their mass-to-charge ratio and the primary RF amplitude. Interactions with the collision gas are important in the trap because it extracts energy from the ions and causes retention of a certain portion of the ions injected in the trap.

2.2. Thermal Analysis and Techniques

2.2.1. Thermal Analysis

Thermal Analysis (TA) encompasses a wide range of techniques that includes the following factors: the sample, the reagent (heat), and the signal.[11] Thermal Analysis, as published by the International Confederation for Thermal Analysis and Calorimetry

(ICTAC), is defined as a group of techniques in which a property of the sample is monitored against time or temperature while the temperature of the sample, in a specified atmosphere, is programmed.

The two primary methods of TA used in this study are Thermogravimetric Analysis (TGA) and Differential Scanning Calorimetry (DSC). It is important to note that there are some factors that affect the overall success of TA experiments, and must be stated.[11] These factors include: 1). a chemical description of the sample, including source, purity, and any other pretreatment of the sample; 2). a description of the crucible along with its shape and the type of material; 3). the rate of heating; 4). the atmosphere around the sample; and 5). the mass of the sample. Copper sulfate pentahydrate is a common calibration standard used for both the TGA and DSC and is displayed in figure 2.3. Figure 2.3 also illustrates the effects of sample size for a TGA experiment.

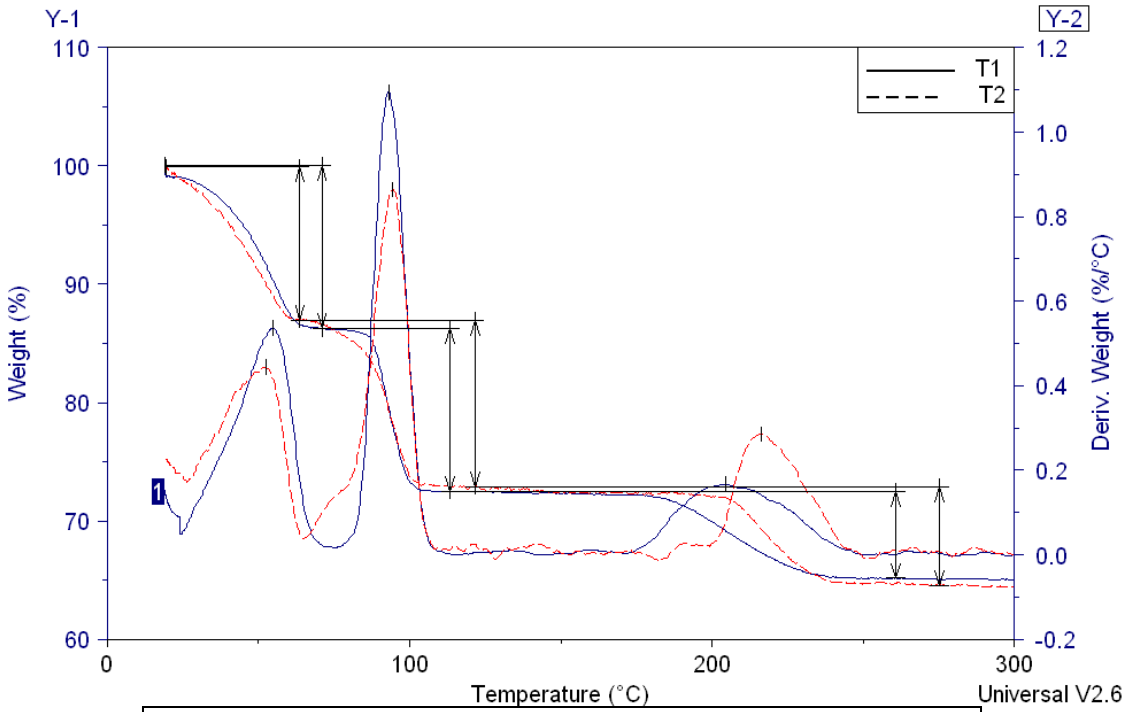

Figure 2.3: TGA and 1st derivative of Copper sulfate pentahydrate.

The plateau of the TGA curve, which is blue in color (solid line), has increased with the increase in mass compared to the TGA curve in the red (dotted line). The slope of the derivative TGA curve, which is also presented in figure 2.3, is also different where the peak max has shifted and the area has changed. In figure 2.3, the loss of water is observed in three stages corresponding to mass percent losses of 14.42%, 14.42%, and 7.21%. These mass percent losses account for the loss of two water molecules in the first stage, the loss of two water molecules in the second stage, and the loss of one water molecule in the final stage to yield copper sulfate. Table 2.1 summarizes the observed mass losses and the temperature range.

Compound	Sample	Temperature Range	Mass % loss
$CuSO_4$-5H_2O	T1	19 to 71°C	13.82
		71 to 113°C	13.76
		113 to 150°C	7.34
	T2	19 to 64°C	12.95
		64 to 122°C	14.07
		122 to 150°C	8.36

Table 2.1: Mass % losses from TGA curve of copper sulfate pentahydrate.

2.2.2. Thermogravimetric Analysis

TGA monitors the change in mass of sample as a function of temperature. The general apparatus includes an electrobalance, which is fitted with a thermocouple and furnace, and a computer interface for control. The electrobalance is generally capable of running up to 1.0 g samples, although it must be calibrated regularly to ensure accuracy. In addition to the weight calibrations, temperature calibrations must be preformed since

the thermocouple, which is measuring the temperature of the sample, is not in direct contact with the sample. Temperature calibrations often utilize the Curie or the melting point of a known metal. Figure 2.4 is the Curie point experiment for nickel which is reported at 360.87 °C. Curie point refers to the point where magnetic metal loses it magnetism. By placing a magnet next to the oven on the TGA instrument, the magnetic field causes the sample to gain some mass. The Curie point is reached when there is observed decrease in the gain mass while in the magnetic field.

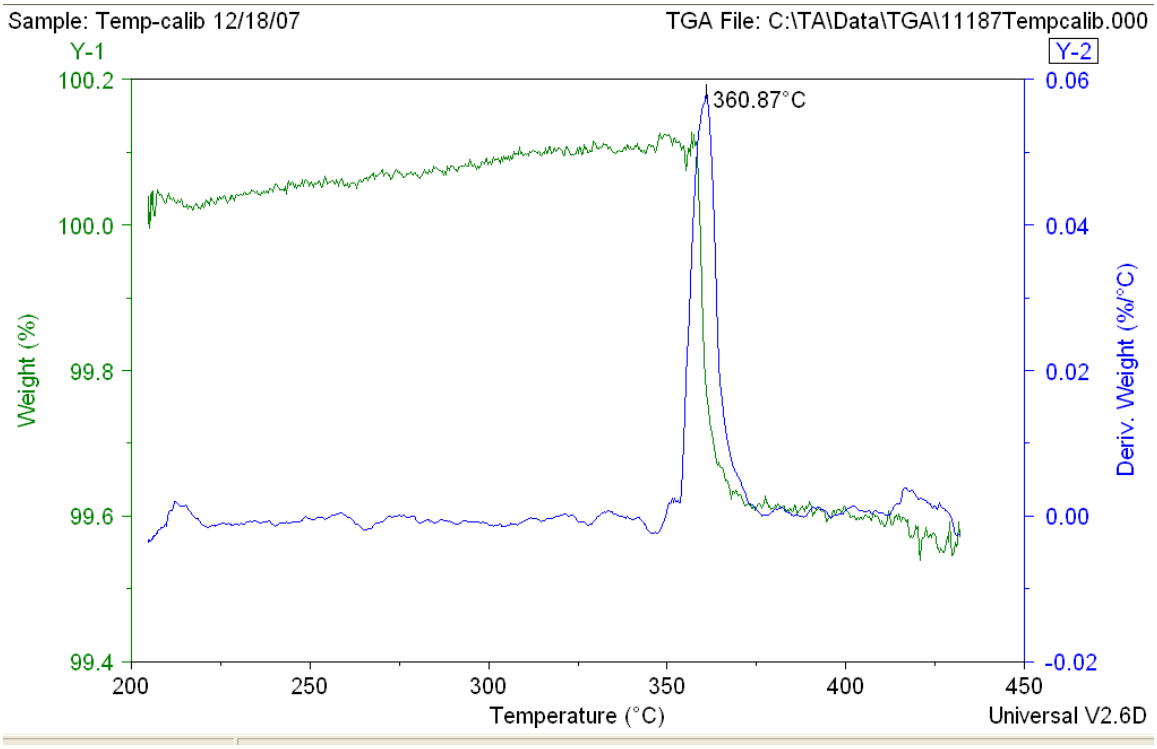

Figure 2.4: Curie point of Nickel.

The atmosphere surrounding the sample of interest is also very important and generally consists of either an inert or oxygen-rich environment. Some experiments also use oxidizing or reducing gases depending on what thermal event is being investigated.[11] The

primary thermal events measured with the TGA includes decomposition, dehydration, and oxidation.

Sample composition also plays a large role in the success of an experiment. For example, even though the sample identity may be of the same chemical composition, if single crystals and fine powders are analyzed, there is likely to be some discrepancy upon heating between each sample.[11] To limit the possibility of explosion and to better control the temperature ramp, sample sizes are generally maintained at a minimum, i.e.: milligram scale.[11] Larger samples will cause the temperature of the sample to become non-uniform through slow heat transfer either via self-heating or self-cooling.

Limited sample sizes also minimize the gas interactions with the surrounding environment.[11] Small powdered samples that are uniformly thin have been found to give the best results.[12] The temperature ramp used in the analysis will depend on the sample size (as the rates of heat transfer differ), physical changes, and reactivity.[5] Depending on the heating curve, several interpretations can be made. The main type of curve in this study involves single stage decomposition where one can define the reactant stability limit, determine the stoichiometric ratios, and investigate the kinetics of the reaction by following the rate of mass loss versus time.[11] In this study, each recorded TGA spectrum is a fingerprint for the compound where the labeled steps corresponds to some mass loss. The recorded mass spectrum of each compound provides a fragmentation pattern which illustrates stability and relaxation pathways. While each technique has its own specific advantage, an independent analysis of both thermogravimetric and mass spectrometric results will be made with a comparison where appropriate.

2.2.3. Differential Scanning Calorimetry

DSC involves heating a sample and a reference, both in pans, through some programmed temperature ramp while measuring the difference in heat flow between the sample and reference. This technique is different from TGA in that it measures phase changes, and both endothermic and exothermic processes. Figure 2.5 is the general schematic of a DSC instrument.

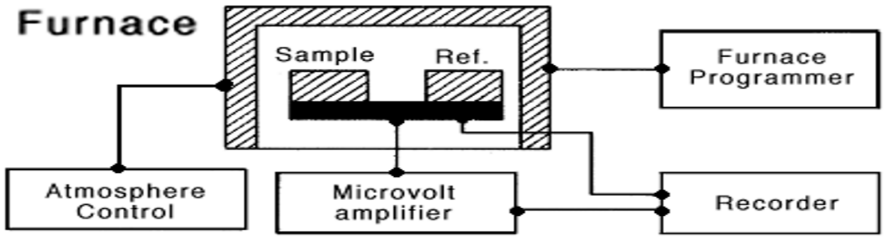

Figure 2.5 General schematic of power modulated DSC.

The instrument used in this study heats the sample and reference pan from the same source where the temperature difference between the pans is measured and converted to measurable power difference. Calibration of the temperature scale, the power scale, and of the reference pan is regularly done using metals with known melting points. Figure 2.6 is the melting point of zinc where the melting and fusion processes are shown by the presence of an endothermic peak and then exothermic peak in the reverse direction.

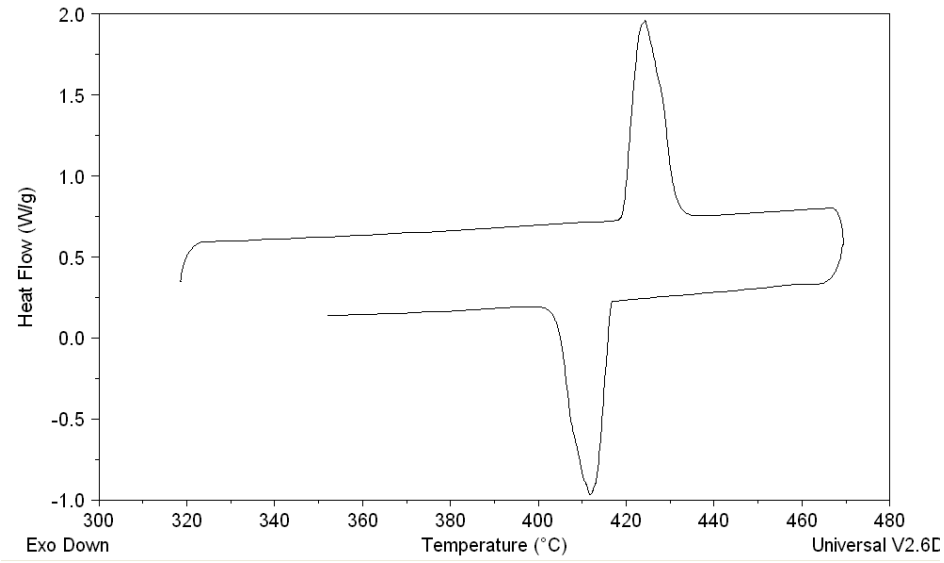

Figure 2.6: DSC of Zinc.

Alumina pans are often used in DSC measurements since they have a moderately high melting point and low reactivity.[11] Samples are also kept to a minimal size, since the pans are usually sealed. Ideally the sample should be uniformly placed and kept compact if possible on the surface of the pan to ensure good surface contact. Dense compact powders are preferred when running DSC experiments. When conducting DSC experiments, the results are often times correlated with results of the corresponding TGA experiment.[11] DSC was employed in this study to measure melting and boiling points.

2.3. Comparison MS and TA

Before a worthwhile comparison can be made between MS and TA, it is important to reiterate how each sample is analyzed. In MS, the species are ionized, where ions of increased stability is detected. In TA, the species are heated until they decompose yielding mass losses until the sample is completely gone. The observed mass percent loss

for the TGA curve corresponds to what is left from the sample which allows for a possible degradation pathway to be proposed. If the mass of a particular fragment observed in MS is similar to the recorded mass percent loss for the TA data, then one can potentially correlate the data and extract the major fragmentation pathway for that particular compound. It is important to note that TA is a very sensitive technique where slight subtleties in the data can be misinterpreted and/or remain inconclusive.

2.4. Natural Product Chemistry

Natural product chemistry includes any substance that is found nature that has some pharmaceutical or biological importance. By investigating how to synthesize these types of molecules in bulk and in a laboratory, it may prove be less expensive than trying to extract the compound from a natural source. Chiral molecules are very important in the synthesis of natural product molecules. Carbohydrates are excellent sources of chiral carbons and are one the most abundant classes of organic molecule on the planet. By starting with cheap and readily available carbohydrates, the overall synthesis is very cost efficient. The two molecules investigated in this study are the first two steps to the synthesis of a diazoester. The diazoester is then used in metal-catalyzed decomposition reaction. We wanted to investigate the fragmentation and the degradation pathway of both compounds since there is little data in the literature on thermal stability or fragmentation pathway of these two compounds.

2.5. Literature review

The fragmentation and eventual degradation of the simple phenolic compounds were investigated in detail by Fahmey and co-workers in 2001.[2] During their study, they used Electron Ionization Mass Spectrometry and Thermal Analysis techniques to propose acceptable pathways in support of the observed results. By comparing thermal analysis and mass spectrometry data, the authors attempted to support a mechanism leading to the formation of a five-membered ring from an initial six-membered ring phenolic backbone. By investigating phenol, 2-hydroxyphenol (PC), and 2,3-dihydroxyphenol (PG), the fragmentation pathway of PC and PG, as compared to phenol, were investigated using mass spectrometry. From Thermal Analysis, PC was observed to lose two CHO groups successively while PG lost H_2O followed by a loss of CO.

The paper concluded that through a comparative study of the fragmentation by MS and decomposition by TA, the compounds investigated show a similar scheme except in the case of PC where TGA shows a different behavior of the five-membered ring. By identifying the percent mass loss where these molecules decompose, the MS supports the proposed decomposition mechanism. The conclusions in the paper are very important because it shows how TA can support proposed mechanisms for the fragmentation observed in MS.

In a separate study published by Fahmey and co-workers, they investigated the products of a catechol (PC) and pyrogallol (PG) oxidation-reduction reaction with iodine and its derivatives iodate and periodate using MS and TA.[1] Other physico-chemical methods of analyses were used including micro-analytical analysis and infrared

spectroscopy. In this study, the overall goal was to shed light on the identity of the phenolic-iodine oxidation-reduction reaction and suggest a suitable fragmentation and thermal degradation pathway of these compounds. The authors state in this article that it is important for the success of the structural conformation that the comparison is based on the proper choice of the unimolecular fragmentation channel of decay in MS and TA.[1] The authors concluded that by using MS and TA data, coupled with micro-analytical analysis and infrared spectrometry, the proposed structure and general formulae of the phenolic-iodine redox products can be determined. The fragmentation pathway by MS and the decomposition by TA suggest similar pathways until all OH groups and CH_3I molecules are released, after which the pathways then deviate.

Taoana and co-workers published their work on the characterization of cyclopropane-1,1,2-tricarboxylic acid by nuclear magnetic resonance, mass spectrometry, and thermal analysis.[13] The compound was recently synthesized from cyanoacetic acid and 2,3-dibromopropionic acid in a one step procedure under an alkaline medium. In this study, they attempted to explain melting point discrepancies reported in the literature for cyclopropane-1,1,2-tricarboxylic acid. The authors were able to investigate the stability of the compound and from the MS data, they were only able to see the molecular ion in the negative mode. From the TA data, they were able to clarify the discrepancy in the melting point for cyclopropane-1,1,2-tricarboxylic acid. Overall they were able to confirm the structure of the compound and its chemical and thermal stability by comparing to previous results.

In another study by Fahmey and co-workers, mass spectrometry, thermal analysis, and other physico-chemical methods were used to investigate the structure of adrenaline hydrogen tartrate (AHT) and its oxidation-reduction products with iodate and periodate.[14] The main focus was to compare the fragmentation pathway obtained by MS and the decomposition mechanism obtained by TA to confirm the formation of the polymeric products. Microanalyses and infrared spectroscopy were also utilized in the structure confirmation of the starting material and the two products. The authors discussed why the isotope abundances are different based on their respected fragmentation patterns. The authors presented decomposition and fragmentation schemes for all three compounds and discussed the formation of certain fragment ions for the different species and how this compares to the TA data. The authors made other distinct connections from the reaction schemes presented in the paper. Through the formation of certain ions, and by identifying previously investigated behavior, they were able to draw comparisons to the TA data. With these techniques they are able to investigate the behavior of AHT and further support, for some species, how MS and TA data can be compared. Mass spectrometry provides the structural information in the gas phase and thermal analysis provides the quantitative fragmentation in the solid state.

Corbi and co-workers characterized a new platinum(II) complex with L-mimosine using ^{13}C NMR, ^{15}N NMR, infrared spectroscopy, mass spectrometry, and thermal analyses.[15] From the MS data they were able to explore the fragmentation pathway which supports the proposed structure and formula for the new complex. From the TA data, they were able to further characterize the new complex by monitoring the water loss and oxidation process taking place (TGA data). The authors later confirmed the product of the

oxidation of the new complex using powder X-ray diffraction. From the DSC data, they observed a strong exothermic peak and some weak exothermic peaks, which were later assigned to ligand oxidation of the complex in two steps. In this article there was no comparison between the MS data and TA data, but characterization of the new compound was achieved.

In some more recent studies, semi empirical molecular orbital (MO) calculations were utilized in conjunction with MS and TA data. MO calculations helped in the selection of a suitable thermal degradation pathway occurring in TA and fragmentation pathways in MS. Zayed and co-workers published a study where they investigated the drug diazepam using TA, MS, and MO calculations to provide a more thorough correlation between its chemical behavior and the electronic structure of the drug.[16] They stated that there is no study on the thermal stability of this drug with temperature changes in the literature.[16]

During their investigation, Zayed and co-workers performed EI-MS at both 70eV and 20eV. The authors used such different ionization energies to minimize fragmentation in an attempt to simplify the analysis. The observed TA data was coupled with a kinetic analysis of the drug and MO calculations were performed on the neutral drug molecule and the charged molecule to correlate with fragmentation pathways and thermal degradation. The main focus of the study was to gain quantitative and qualitative information on the structure-activity relationship for diazepam. With this study, they were able to further support the applicability of MS and TA data while also supporting the use of MO calculations. The authors concluded that from the theoretical and data

comparison, the primary fragmentation pathway of diazepam was the loss of CO. The authors also noted that the theoretical data and experimental data did not always agree, and this alone can suggest the overall complexity of the drug.[16]

In another study, M.A. Zayed et al. investigated transition metal codeine phosphate complexes using infrared spectroscopy, magnetism, and reflectance data to compare to MS fragmentation and TA decomposition.[17] They attempted to determine the structural formulae of the prepared complexes and used MS and TA to support their proposed structural formulae. The data provided information on the molecular weight of the complexes under investigation, information on the thermal behavior, fragmentation patterns, and stable molecular ions.[17]

In a similar study, M.A. Zayed and co-workers conducted a study on transition metal codeine complexes using MS and TA, but also included MO calculations.[18] Very little work was previously reported in literature for the thermal degradation pathway of codeine. While codeine has been studied extensively by MS, a comparison between MS and TA data, coupled with MO calculations, was done to connect the chemical behavior of the drug and its electronic structure. This study also allows for the analysis of codeine's tendency to form complex structures with the d-block elements and to investigate the stability of such complexes with correlation to its medical uses. In this study, the authors state that extensive information about the active site responsible for its chemical, biological, and medical uses of codeine is needed in order to achieve the best results when computing the MO calculations.

Previous studies by Zayed et. al., mentioned earlier in the review, investigated the tendency of transition metals to complex with codeine using a combination of physico-chemical methods and observed very high stability for the formed complexes.[18] By comparing their results from this study to others, they could better understand the biological role the drug and its complexes play. For the comparison of simple phenolic compounds, MS and TA seem sufficient for simple process identification.[2] In this study, the authors also explained why they used MO calculations in some studies and not in others.[18] For more complex molecules, however, many more dissociation/fragmentation channels open making the analysis very involved. The authors were able to gain valuable information from this study and were able to accurately identify the fragmentation and thermal degradation pathway of the pure drug. They also were able to compare these findings to their previous comparison using MS and TA on d-block elements complexes with codeine. In most of the complexes investigated, the comparison was valid in selecting suitable fragmentation pathways for the complexes.[18] An important conclusion from their work relates the loss of a hydroxyl group in MS to the loss of water in TA.[18]

In a separate study conducted by Zayed et. al., they preformed a structural investigation study on the drug stertraline and its iodine product using a comparison of MS and TA coupled with MO calculations to help understand the biological reactivity of the drug.[19] They were also able to compare the behavior and stability of sertaline and the sertaline-iodine product as a neutral and ionic species. They preformed their study with other physico-chemical methods of analyses including IR, ^{1}H-NMR, ^{13}C-NMR, and microanalyses. By combining these techniques, the authors gained some understanding in the stability of the drug under thermal degradation in the solid form. They were also able

to predict the primary fragmentation site of both stertraline and the iodine product, clarify the subsequent bond cleavage, and develop an appropriate thermal degradation scheme. From this information, they could gain a better understanding of the biodegradation of the drug and its iodine product. The authors were also able to analyze the changes that occur in the MS and TA data when iodine inserted into the drug. This change is confirmed by the difference in its heat of formation, dipole moment, electron affinity, and its ionization potential. The comparison with the MO calculations gave insight into the nature of the bond ruptures that occur in the neutral and the ionic modes of both sertaline and its iodine product.

Chapter 3. Experimental

3.1. Materials

3.1.1. Phenols Derivatives and Diacetone-D-Glucose

Most of the compounds under investigation were ordered from Aldrich and Acros. 2,6-Dimethylphenol, *p*-cresol, and 2-ethylphenol were from Acros, and 3,5-dimethylphenol and diacetone-D-glucose were from Aldrich. All compounds, except for 2-ethylphenol, came as a pure solid whereas 2-ethylphenol was a pure liquid. The sample purity for the phenolic derivatives was tested by LC/MS. The purity of diacetone-D-glucose was also tested by LC/MS, NMR, and IR.

3.1.2. Synthesis of 2-phenylacetyl ester

To a 250 mL flame-dried round bottom flask was added 2.026 g of diacetone-D-glucose. 1.181 g phenyl acetic acid and 0.222 g DMAP was added to the round bottom flask. 20 mL of dry CH_2Cl_2 and 20 mL of dry CH_3CN was added to the round bottom flask. Then 10 mL of DCC was added dropwise over a period of 10 mins. The reaction was performed under inert atmosphere. The reaction was allowed to react over a 24 hour period. The solvent was removed by the rotovap and then dried under vacuum. The crude product was recrystallized with ethanol and the isolated yield was 68 %. These conditions are the general conditions for an esterification.

3.2. Mass Spectra measurements and Instruments

3.2.1. The Bruker Esquire-LC

The mass spectra for *p*-cresol, 2-ethyphenol, 2,6-dimethylphenol, 3,5-dimethylphenol, diacetone-D-glucose, and the 2-phenylacetyl ester were run on the Bruker Esquire-LC mass spectrometer. The phenol derivatives were recorded using APCI method of ionization in methanol and the glucose derivatives were recorded using the ESI method of ionization in acetonitrile. The instrument was calibrated with ES Tuning Mix for LC/MSD Ion Trap in 100 mL acetonitrile solution from Agilent. The samples were inserted directly to the ionization chamber bypassing the LC part of the instrument. The experiments were performed multiple times.

3.2.2. GCQ/ Electron impact ionization, Direct Insertion Probe

The mass spectra of the phenol derivatives were also recorded using the Finnigan GCQ with Direct Insertion Probe. The direct insertion probe was fitted to run liquid samples with a ramp of 10 mA/s up to 600 mA/s to volatize the samples. The ion trap was held at 70 eV. The calibration was done with perfluoro-kerosene. The phenol derivatives were dissolved in methanol to make a 5.0 molar solution. The experiments were performed multiple times.

3.3. Thermal Analyses (TGA and DSC) measurements and instruments

3.3.1. TGA

The TGA measurements were preformed with TA Instruments TGA model 2050. The phenol derivative samples were run untreated from the chemical supplier. 2-ethylphenol was in liquid form while all other phenol derivatives were solids. The samples (5 mg to 10 mg) were run from room temperature to 300 °C. The ramp for the phenol derivatives was 5 °C/min. The carbohydrates were run under similar conditions with a temperature range from room temperature to 350 °C for diacetone-D-glucose and from room temperature to 450 °C for the 2-phenylacetyl ester. The ramp for the carbohydrates was 5 °C/min. Standard alumina pans were used for all experiments. Nitrogen gas was used for the surrounding atmosphere and several calibrations were preformed on the instruments including the Curie point for nickel, the decomposition of copper-sulfate pentahydrate, and the decomposition of calcium oxalate. Figure 3.1 is a TGA and 1st derivative curve for calcium oxalate at 10 mg and 5 mg.

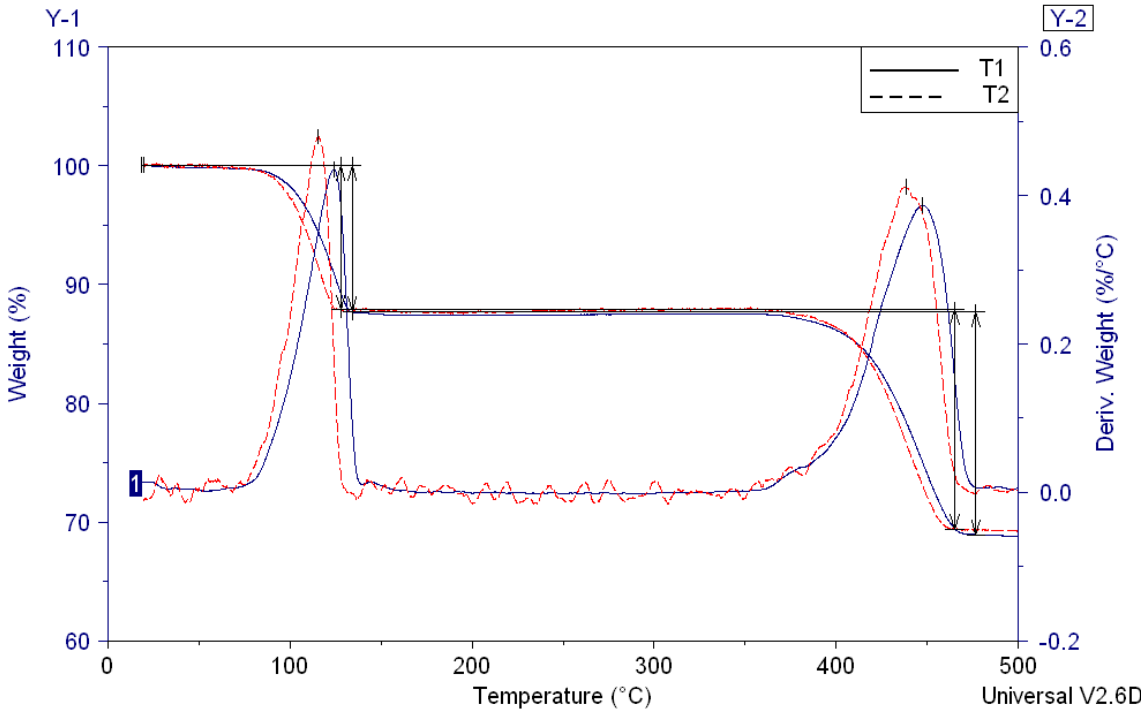

Figure 3.1: TGA and 1st derivative curve for Calcium Oxalate.

Reaction scheme 3.1 illustrates the observed dehydration of calcium oxalate followed by a loss of carbon monoxide to yield calcium carbonate with mass percent losses of 12.32% and 19.16% respectively.

$$CaC_2O_4 \cdot H_2O \xrightarrow{-H_2O} Ca_2C_2O_4 \xrightarrow{-CO} CaCO_3$$

Scheme 3.1: Decomposition of calcium oxalate monohydrate.

The final decomposition was not measured because it exceeded the temperature range of the instrument. Table 3.1 summarizes the observed mass percent losses and all experiments were preformed multiple times.

Compound	Sample	Temperature Range	Mass % loss
$CaC_2O4 \cdot H_2O$	T1	19 to 134°C	12.37
		134 to 477°C	18.75
	T2	19 to 128°C	12.2
		128 to 465	18.49

Table 3.1: Observed mass % losses for calcium oxalate monohydrate.

3.3.2. DSC

The DSC measurements were preformed with TA Instruments DSC model 2910. The phenol derivatives, 2 mg to 15 mg samples, were run from 32 °C to 300 °C at a ramp rate of 5 °C/min. The phenol derivatives were used as is. As stated earlier, 2-ethylphenol is in liquid form and the other phenol derivatives are in solid form. The carbohydrate samples were both in solid form and were assumed to be pure based on NMR and IR. The samples (2 mg to 10 mg) were run from 32 °C to 350 °C for diacetone-D-glucose and to 450 °C for the 2-phenylacetyl ester at a ramp rate of 5° C/min. A multiple point calibration was performed using indium, zinc, and tin. The samples were run in an alumina sealed pan and also in an open alumina pan. Nitrogen gas was used for the surrounding atmosphere and all experiments were preformed twice.

3.4. Other Instruments

The ^{1}H-NMR for the carbohydrate compounds were run on the Bruker Avance 400 NMR in $CDCl_3$. The IR for the carbohydrate compounds were run on the Thermo IR 200 Spectrometer. Salt plates were used and the solid samples were dissolved in $CDCl_3$.

Chapter 4. Mass Spectra Analysis

4.1. Phenol Derivatives

4.1.1. *p*-Cresol

The negative APCI mass spectrum for *p*-cresol is displayed in figure 4.1 and shows an intense $(M-1)^-$ peak at m/z 107, where M is the molecular ion, and a slight peak at m/z 123.

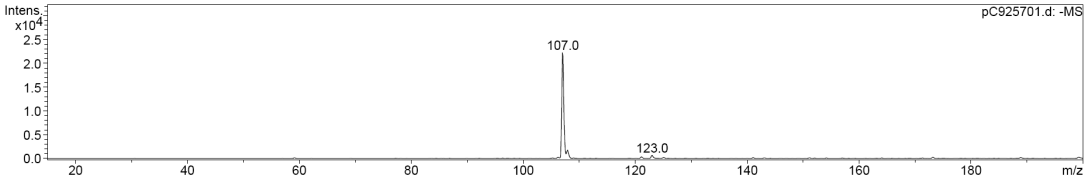

Figure 4.1: Negative APCI mass spectrum of *p*-cresol.

When using the GCQ under EI conditions, the fragmentation patterns are very different. Most phenolic compounds display many fragments under EI analysis with the molecular ion usually being present. When alkyl substituted phenols were analyzed, the molecular ion and the loss of hydrogen, ie: (M-H) was observed in high abundance.[3] The EI mass spectrum of *p*-cresol is presented in figure 4.2 and shows an intense molecular ion and (M-H) peak at m/z 108 and 107 respectively. Proposed fragmentation pathways for *p*-cresol are included in Scheme 4.1. Table 4.1 lists the observed fragments along with relative intensities.

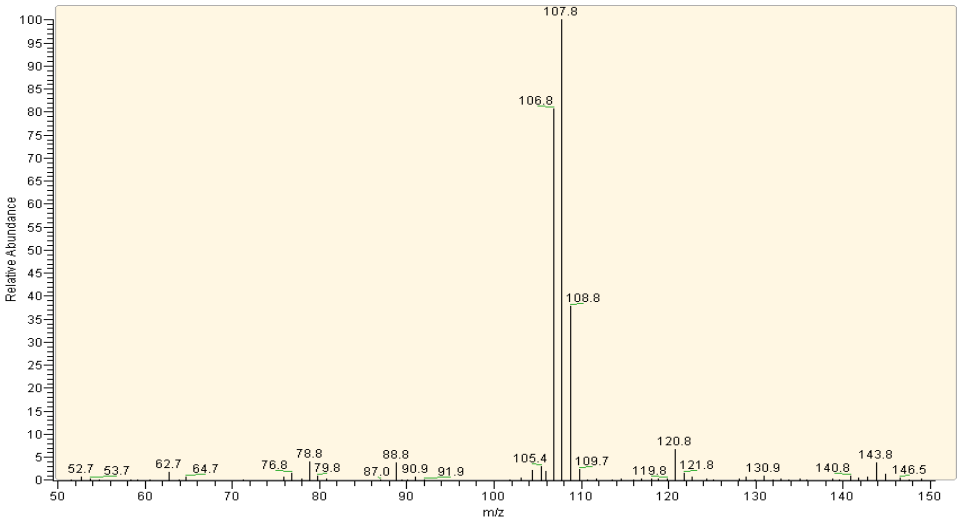

Figure 4.2: GCQ-EI mass spectrum of *p*-cresol

The peak at m/z 107 in figure 4.2 is likely due to the loss of one benzylic hydrogen atom.[20] The presence m/z 107 however, can be attributed to the formation of both the oxonium ion and the resonance stabilized hydroxytropylium ion. Scheme 4.1 proposes the structure of the predominant ions where the presence of the oxonium ion can be described by the *para* effect with the alkyl group *para* to the phenolic hydroxyl group.[4] Via the resonance stabilized hydroxytropylium ion, the loss of a CO group results in the formation of the benzylium type ion at m/z 79 with a relative intensity of 4.96%. The loss of H_2O from the oxonium ion would result in $C_7H_6^+$ with m/z 89 and relative abundance of 4.37%.

Compound	Fragment	m/z	Relative Intensity
***p*-cresol**	$[M^{+\bullet}]$	108	100
	$[M^{+\bullet} - H]$	107	76.39
	[M+• - H] - OH	91	0.94
	$[M^{+\bullet} - H] - H_20$	89	4.37
	$[M^{+\bullet} - H] - CO$	79	4.96
	$[M^{+\bullet} - H] – CO - H_2$	77	1.32
	$[M^{+\bullet}] - CH_3CO$	65	0.29

Table 4.1: List of fragments for *p*-cresol.

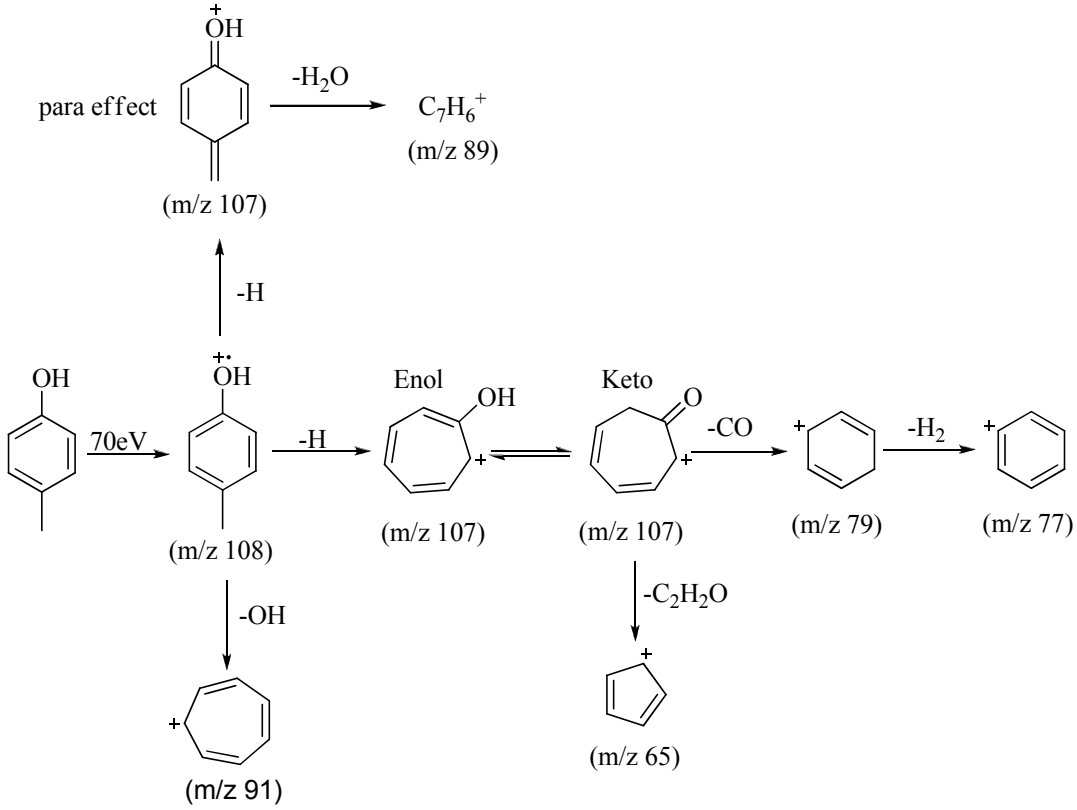

Scheme 4.1: Proposed fragmentation pathway for *p*-cresol.

The benzylium ion at m/z 77, with a relative intensity of 1.37, is due to the loss of molecular hydrogen.[20] The fragment observed at m/z 65, relative intensity at 0.29%, is due to the loss of a methyl group, which is in accordance with Stevenson's rule, and then

the loss of CO due to a ring rearrangement.[4] There is also a peak at m/z 91, with a relative intensity at 0.94, which is due to the loss of a hydroxyl group from the molecular ion. The fragment at m/z 89 with a relative intensity of 4.37% supports the presence of the oxonium ion.

4.1.2. 2-Ethylphenol

The negative APCI mass spectrum for 2-ethylphenol is displayed in figure 4.3 and shows an intense peak at m/z 121 $(M-1)^-$ and a smaller peak at m/z 106 $(M-OH)^-$.

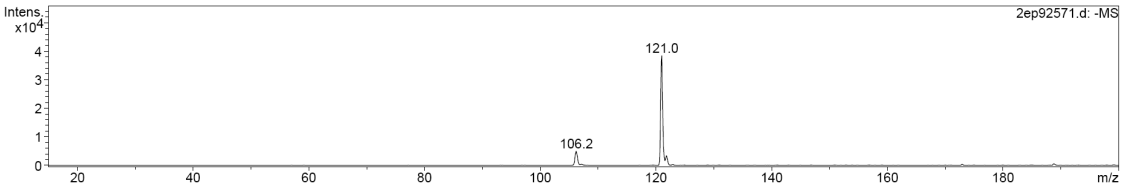

Figure 4.3: Negative APCI mass spectrum of 2-ethylphenol.

The positive EI mass spectrum for 2-ethylphenol is presented in figure 4.4 and the molecular ion peak and the loss of a benzylic hydrogen atom $[M^{+\bullet}- H]$ peak is observed at m/z 122 and 121, respectively. Table 4.2 summarizes the relative abundances of the predominant fragments displayed in figure 4.4.

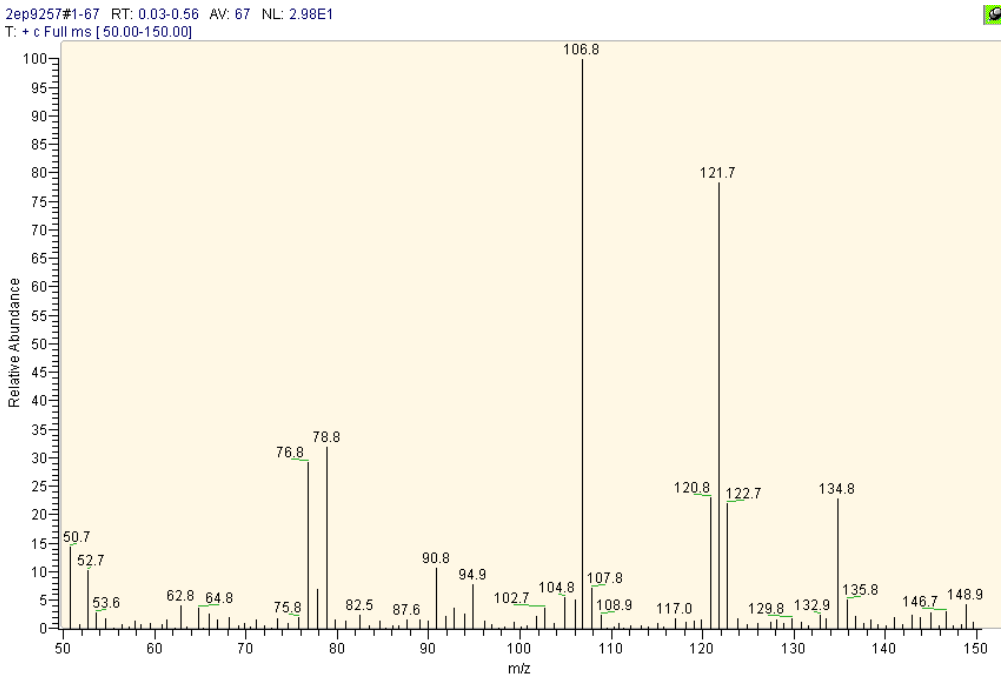

Figure 4.4: GCQ-EI mass spectrum for 2-ethylphenol.

Compound	Fragment	m/z	Relative Intensity
2-ethylphenol	$[M^{+\bullet}]$	122	69.02
	$[M^{+\bullet} - H]$	121	13.78
	$[M^{+\bullet}] - CH_3$	107	100
	$[M^{+\bullet} - H] - H_2O$	103	3.76
	$[M^{+\bullet}] - CH_2OH$	91	11.85
	$[M^{+\bullet} - CH_3] - H_20$	89	1.33
	$[M^{+\bullet} - CH_3] - CO$	79	36.97
	$[M^{+\bullet} - CH_3] – CO - H_2$	77	32.87
	$[M^{+\bullet} - CH_3] - C_2H_2O$	65	3.88
	$[M^{+\bullet} - CH_2OH] - C_2H_2$	63	4.19

Table 4.2: List of fragments for 2-ethylphenol

In the mass spectrum of 2-ethylphenol, the base peak at m/z 107 is partially due to the hydroxytropylium ion being present. The loss of a methane radical, due to homolytic cleavage from 2-ethylphenol, would result in the presence of m/z 107.[3] The *ortho* effect

is also observed in the mass spectrum of 2-ethylphenol, where the loss of water would give a peak at m/z 103. The relative abundance of this proposed structure from the *ortho* effect is 3.76%.[3]

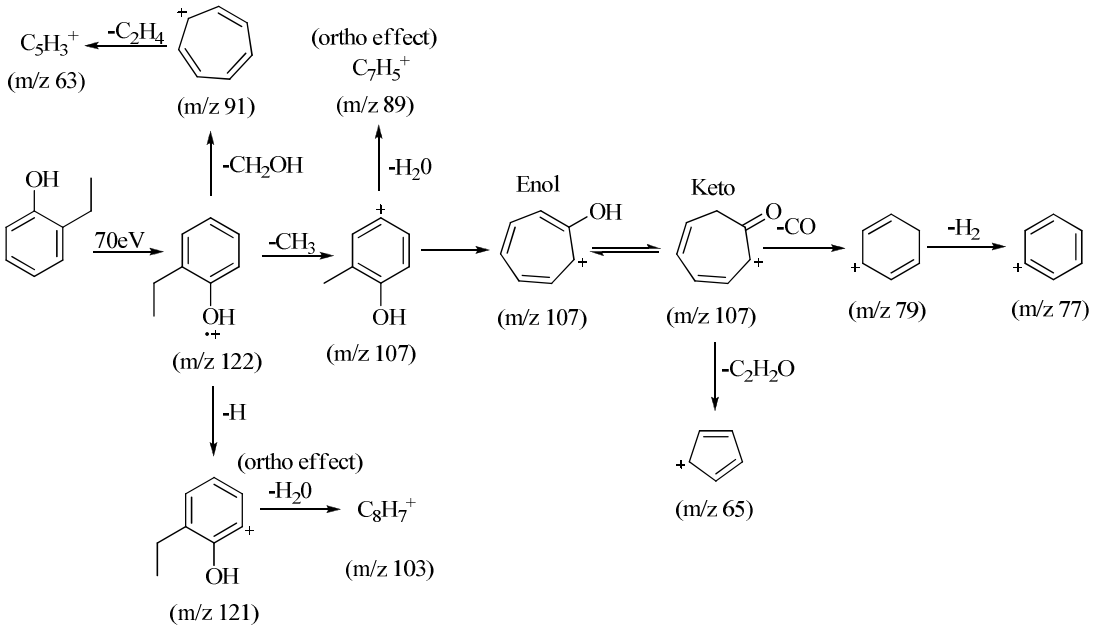

Scheme 4.2: Proposed fragmentation pathway for 2-ethylphenol.

From Scheme 4.2, the *ortho* effect also can be observed for m/z 89 which corresponds to the loss of H_2O following the loss of a methyl radical from the molecular ion. This behavior is also observed in the mass spectrum of 2,6-dimethylphenol.

The pathway leading to the structure with m/z 91 in scheme 4.2, which has a relative intensity of 11.85%, is due to some rearrangement which results in the loss of CH_2OH, yielding the tropylium ion.[3] The formation of the hydroxytropylium ion can tautomerize to the keto form which allows the loss CO with a peak at m/z 79. A loss of molecular hydrogen, which was also observed in the case of *p*-cresol, can account for the peak at m/z 77. Similar to m/z 65 for *p*-cresol, the formation of this fragment from 2-

ethylphenol corresponds to a loss of a methyl group and then a loss of C_2H_2O. This peak has a relative intensity of 3.88%.

4.1.3. 2,6-Dimethyl phenol

The positive and negative APCI mass spectrum for 2,6-dimethylphenol is shown in figures 4.5 and 4.6, respectively. Figure 4.5 contains an intense peak at m/z 123 which corresponds to $(M+1)^+$, a peak at m/z 108, which is the loss of a methyl group $(M-CH_3)^+$, and a peak at m/z 95, which is a loss of CO from the molecular ion $(M-CO)^+$. The benzene ion $(M-C_2H_6O)^+$ is also observed at m/z 77. In the negative APCI mode, which is displayed in figure 4.6, there is an intense $(M-1)^-$ peak at m/z 121 an another unassigned peak at m/z 135.

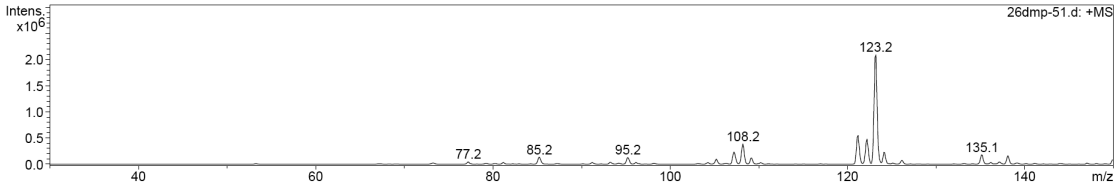

Figure 4.5: Positive APCI spectrum of 2,6-dimethylphenol.

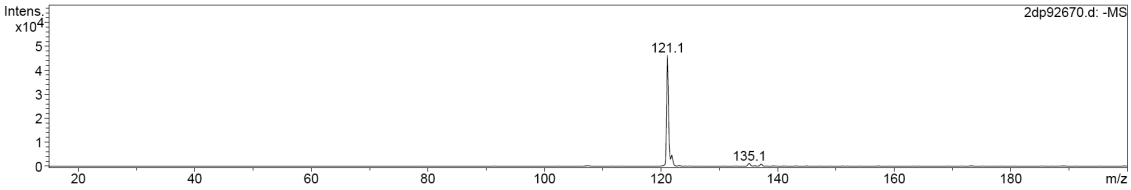

Figure 4.6: Negative APCI spectrum of 2,6-dimethylphenol.

In the GCQ-EI mass spectrum of 2,6-dimethylphenol, presented in figure 4.7, we observed a similar pathway to that of 2-ethylphenol, except the relative intensity of the fragments.

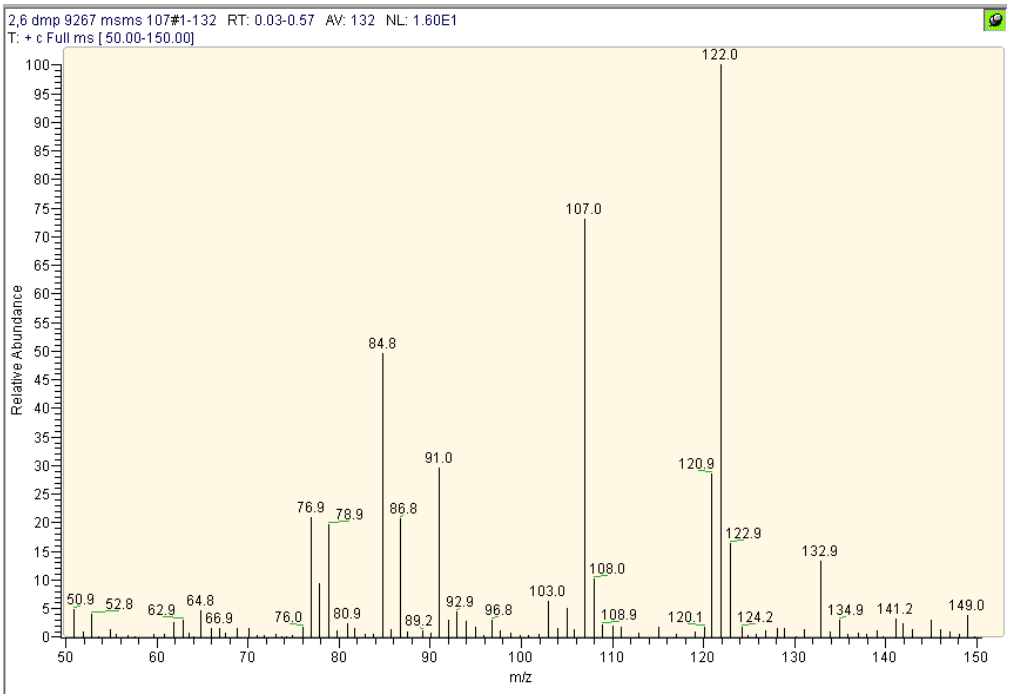

Figure 4.7: GCQ-EI mass spectrum of 2,6-dimethylphenol.

In EI mass spectrum of 2,6-dimethylphenol, the most intense peak is the molecular ion peak at m/z 122. The peak corresponding to $[M-H]^+$ is also observed at m/z 121, with a relative intensity of 28.5%. The loss of methyl radical is also observed in the fragmentation pattern of 2,6-dimethylphenol. The $[M-CH_3]^+$ peak at m/z 107 has the second largest relative intensity at 73.06%.

Compound	Fragment	m/z	Relative Intensity
2,6-dimethylphenol	$[M^{+\bullet}]$	122	100
	$[M^{+\bullet} - H]$	121	28.5
	$[M^{+\bullet}] - CH_3$	107	73.06
	$[M^{+\bullet} - H] - H_2O$	103	6.3
	$[M^{+\bullet}] - CH_2OH$	91	29.55
	$[M^{+\bullet} - CH_3] - H_20$	89	1.09
	$[M^{+\bullet} - CH_3] - CO$	79	19.79
	$[M^{+\bullet}] - C_2H_5O$	77	21.02
	$[M^{+\bullet} - CH_3] - CO - H_2$	65	4.69
	$[M^{+\bullet} - CH_2OH] - C_2H_2$	63	3.08

Table 4.3: List of Fragments for 2,6-dimethylphenol.

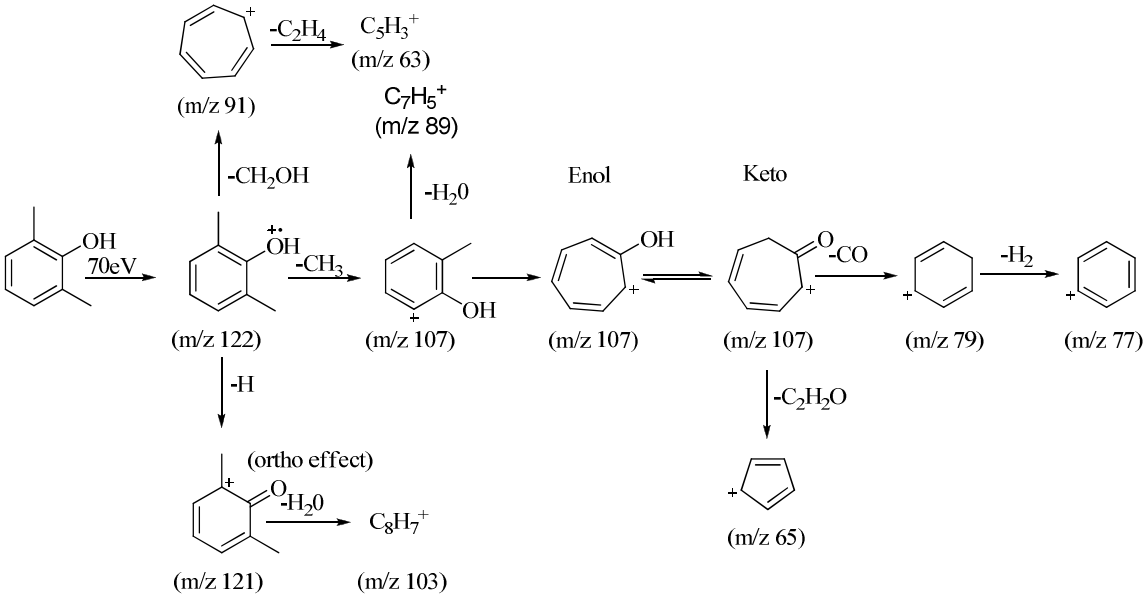

Scheme 4.3: Proposed fragmentation pathway for 2,6-dimethylphenol.

From scheme 4.3, the proposed structure for m/z 103, with a relative intensity of 6.3% from mass spectrometry, is due to the *ortho* effect. A similar pathway is observed for *p*-cresol, in that there is a peak observed at m/z 89 with a relative abundance of 1.09% due to the *ortho* effect also. The tropylium ion, which corresponds to the proposed structure at m/z 91 in scheme 4.3, has a relative intensity of 29.55% from Table 4.3, is

due to the loss CH_2OH from the molecular ion. Similar to 2-ethylphenol, there is peak m/z 89 that is also due to ortho effect. After losing the methyl radical, the formation of hydroxytropylium is observed at m/z 107 which later rearranges and loses a CO group at m/z 79. The relative intensity of m/z 79 is 19.79%, suggesting that this process occurs often. The loss of molecular hydrogen is also observed at m/z 77 with a relative intensity 21.02%. The structure at m/z at 65 is due to the loss of a methyl group and then the loss of a C_2H_2O group with a relative intensity of 4.69. Similar to *p*-cresol, a peak at m/z 63 is observed with relative intensity of 3.08. The peak at m/z 63 could be explained by a ring rearrangement with loss of C_2H_2. The relative abundance of m/z 63 is 4.19%.

4.1.4. 3,5-Dimethylphenol

The positive and negative APCI mass spectra for 3,5-dimethylphenol is shown in figures 4.8 and 4.9, respectively. A peak at m/z 123, which corresponds to the $(M+1)^+$ species is observed with other peaks in the spectrum likely background and/or solvent. The spectrum in the negative APCI mode has one peak at m/z 121, and is likely $(M-1)^-$.

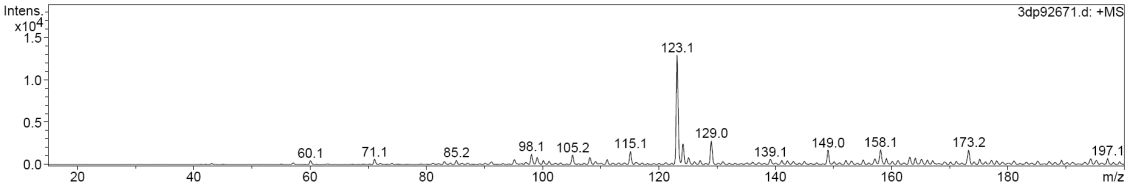

Figure 4.8: Positive APCI spectrum of 3,5-dimethylphenol.

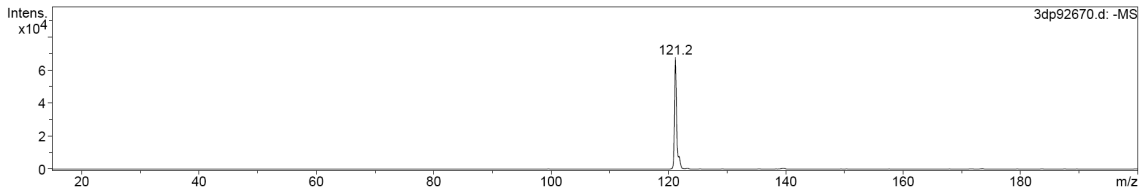

Figure 4.9: Negative APCI spectrum of 3,5-dimethylphenol.

The EI mass spectrum for 3,5-dimethylphenol, presented in figure 4.10 is very similar to that of 2-ethylphenol and 2,6-dimethylphenol, except for the absence of the peak m/z 103. The alkyl substituents are also meta to the hydroxyl group and thus follow a different fragmentation pathway illustrated in scheme 4.4.

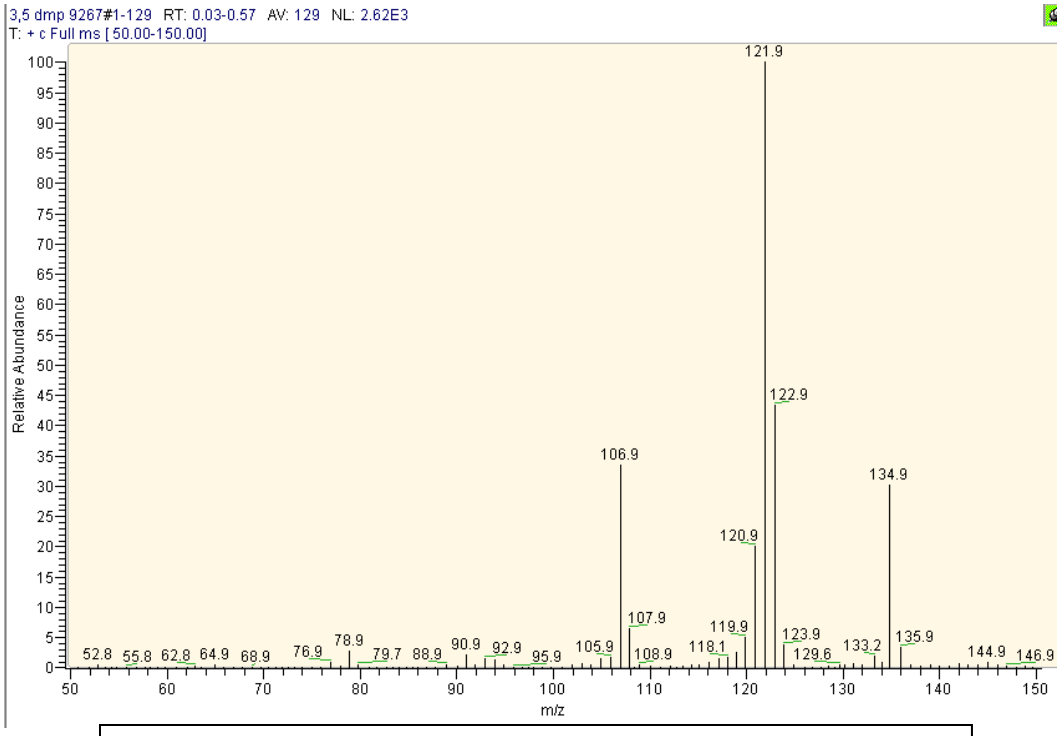

Figure 4.10: GCQ-EI mass spectrum for 3,5-dimethylphenol

For the mass spectrum of 3,5-dimethylphenol, there is an intense molecular ion peak at m/z 122 which is also the base peak. The [M-H] is observed at m/z 121 with relative intensity of 20.28%. The second most intense peak of the spectrum was the [M-CH_3] with a relative intensity of 33.52%. This peak occurs through the loss of methyl radical. Similar to 2-ethylphenol and 2,6-dimethylphenol, the tropylium ion is observed at m/z 91 with relative intensity of 2.26% through the loss of CH_2OH group from the molecular ion. There is a peak observed at m/z 79 with a relative intensity of

2.84%. This peak is due through the loss of a methyl group and then a CO group from the [M-CH_3] peak. As seen in the previous mass spectrum of the phenol derivatives, the loss of molecular hydrogen from the benzylium ion is observed at m/z 77 with a relative intensity of 0.89. Similar to the other phenol derivatives, the peaks at m/z 65 and m/z 63 are observed with a relative intensity of 0.43% and 0.33% respectively. We believe they follow a similar route of fragmentation at the other phenol derivatives investigated in this study.

Compound	Fragment	m/z	Relative Intensity
3,5-dimethylphenol	$[M^{+\bullet}]$	122	100
	$[M^{+\bullet} - H]$	121	20.28
	$[M^{+\bullet}] - CH_3$	107	33.52
	$[M^{+\bullet}] - CH_2OH$	91	2.26
	$[M^{+\bullet} - CH_3] - CO$	79	2.84
	$[M^{+\bullet}] - C_2H_5O$	77	0.89
	$[M^{+\bullet} - CH_3] - C_2H_2O$	65	0.43
	$[M^{+\bullet} - CH_2OH] - C_2H_2$	63	0.33

Table 4.4: List of fragments for 3,5-dimethylphenol.

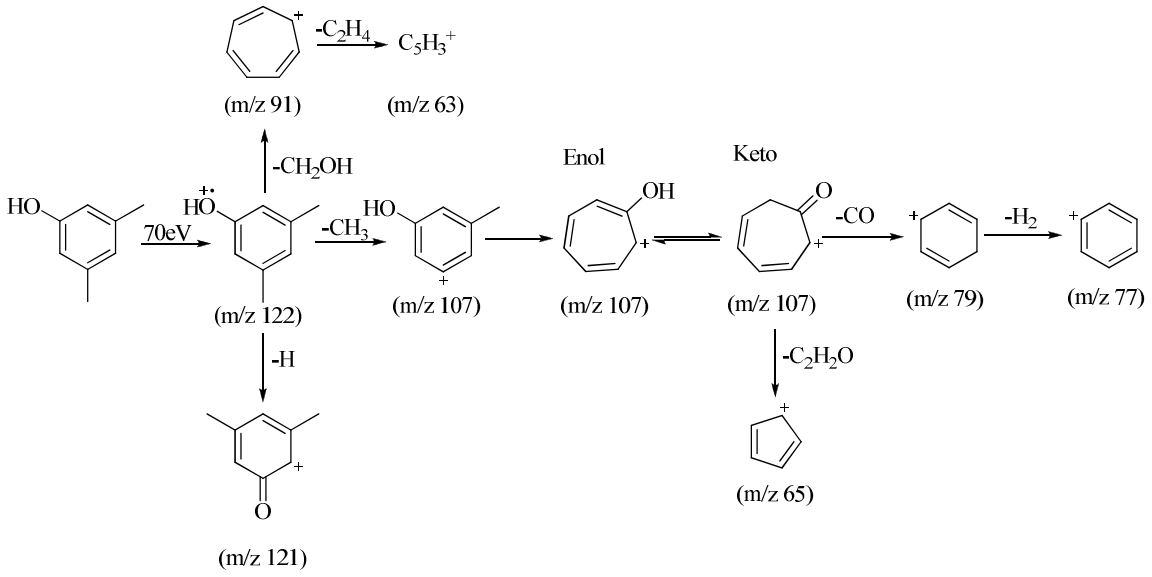

Scheme 4.4: Proposed fragmentation pathway for 3,5-dimethylphenol.

4.2. Diacectone-D-Glucose and 2-Phenylacetyl Ester

4.2.1. Diacectone-D-Glucose

In the mass spectrum for diacetone-D-glucose, the presence of sodium was present on all peaks, which is common to ESI.

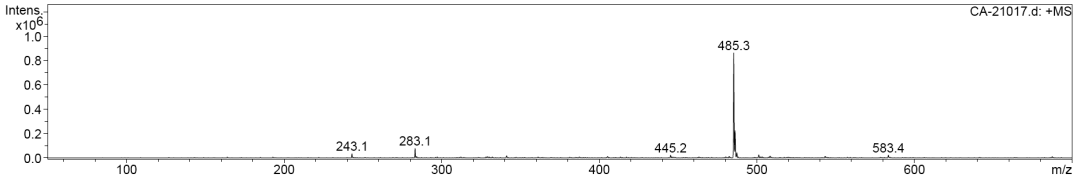

Figure 4.11: Positive ESI mass spectrum of Diacetone-D-glucose.

There is a peak at m/z 283 which is the $[M+Na]^+$ peak. The peak observed at m/z 243 occurs through the loss of C_3H_4. The base peak of the spectrum showed up at m/z 485

and is likely $[(M-C_3H_4)(M)+Na]^+$. This species was formed through the gas phase interaction of the fragments generated upon ionization. The $[(M-C_3H_4)(M)+Na]^+$ ion is also observed to lose a C_3H_4 yielding a peak at m/z 445. The peak at m/z 405 occurs through another successive loss of C_3H_4 from the $[(M-C_3H_4)(M)+Na]^+$ ion. A peak observed at m/z 583 has yet to be assigned.

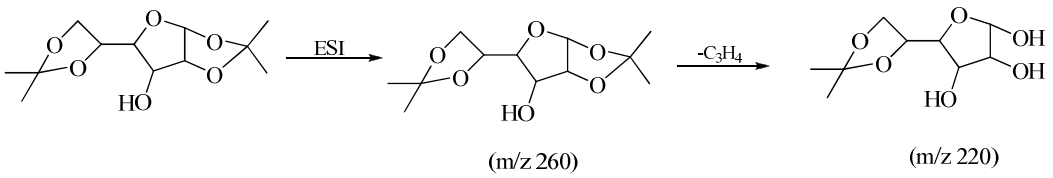

Scheme 4.5: Proposed fragmentation pathway for diacetone-D-glucose.

4.2.2. 2-Phenylacetyl Ester

In the mass spectrum of 2-phenylacetyl ester, the ion exists with sodium also.

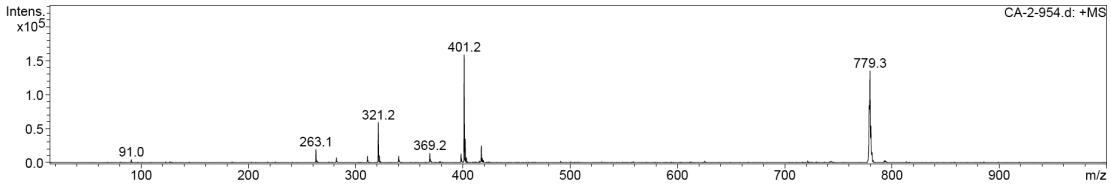

Figure 4.12: Positive ESI mass spectrum of 2-phenylacetyl ester.

The peak observed at m/z 401 is the $[M+Na]^+$ peak while m/z 321 is likely due to the loss of C_2H_3O. The $[M-C_3H_5O]^+$ ion looses another C_3H_5O yielding a peak at m/z 263. The peak observed at m/z 779 is likely the molecular ion dimer with sodium. The peak at m/z 91 is likely due to the fragmentation of a tropylium ion from the molecular ion.

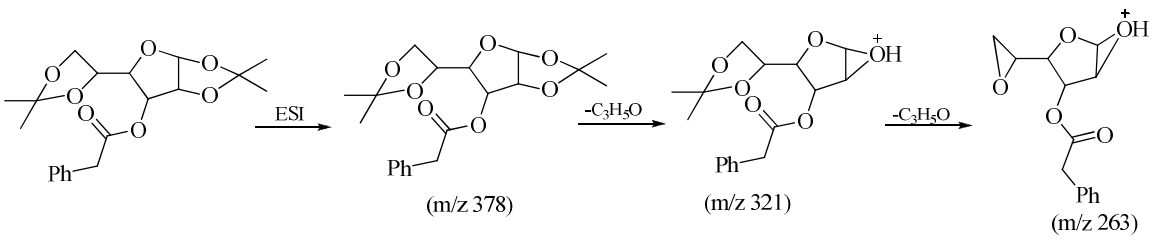

Scheme 4.6: Proposed fragmentation pathway of 2-phenylacetyl ester.

Chapter 5. Analysis of TA data

5.1. Thermal Analysis of phenol derivatives

5.1.1. *p*-Cresol

Thermogravimetric analysis and differential scanning calorimetry were performed on phenol derivatives of varying mass. The temperature range where decomposition was observed to occur had an obvious dependence on mass. Since thermal analysis samples are heated from the outside in, larger sample sizes were found to decompose over a longer time (and temperature range). Figure 5.1 is a single stage decomposition TGA curve for *p*-cresol with the identified inflection points corresponding to specific decomposition steps. Table 5.1 summarizes the temperature range and mass percent loss for each decomposition step proposed for *p*-cresol.

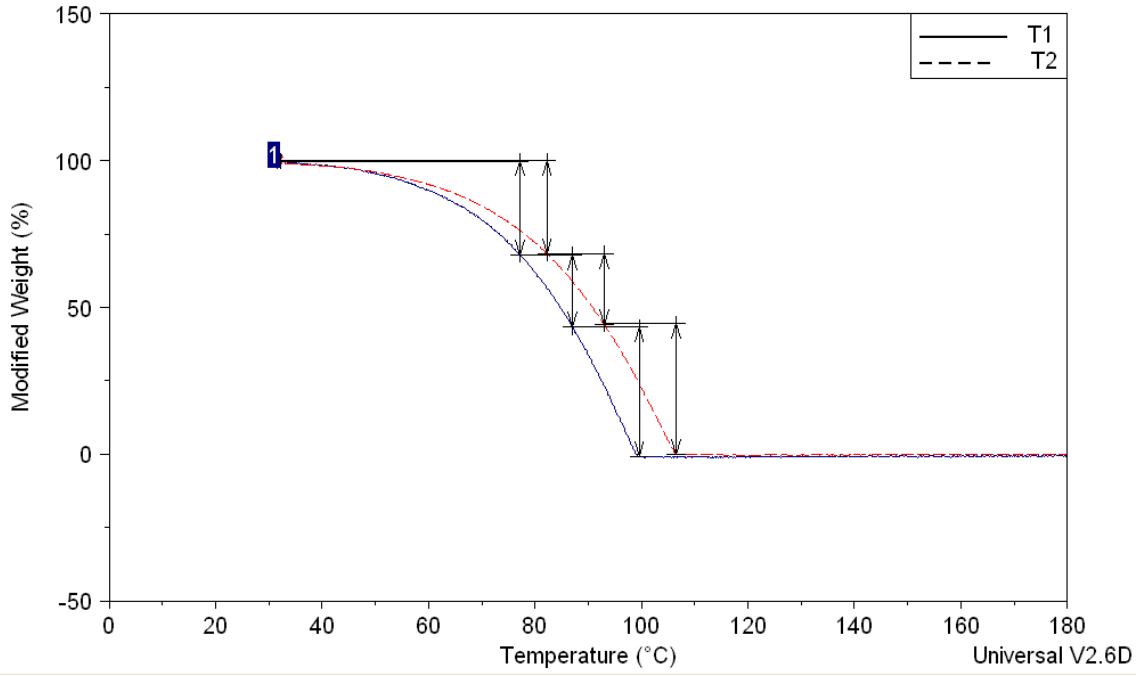

Figure 5.1: TGA curve of *p*-cresol.

Compound	Sample	Temperature Range	Mass % loss
***p*-cresol**	T1	32 to 77 °C	31.93
		77 to 87°C	24.56
		87 to 99°C	44.12
	T2	32 to 82°C	31.66
		82 to 93°C	24.18
		93 to 107°C	44.35

Table 5.1: Onset analysis of *p*-cresol.

The observed mass percent losses corresponding to the inflection points on the TGA curve of *p*-cresol from figure 5.1 are likely due to the loss CH_3 and H_2O in the first step between 32 and 80 °C. The measured mass percent loss for this first step is 31.79 % compared to the predicted mass percent loss of 30.56. The second step of the single stage decomposition of *p*-cresol is observed to include a mass loss of 24.37 % which corresponds very closely to the predicted loss of 24.07 % from C_2H_2. Scheme 5.1 summerizies the proposed successive mass loss for *p*-cresol.

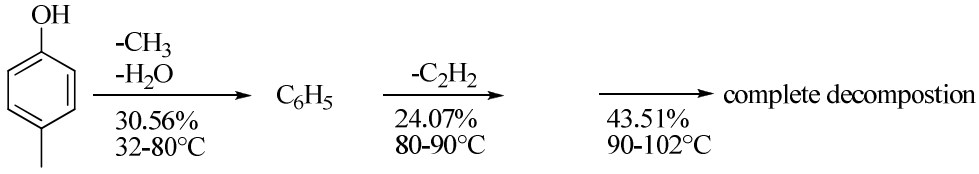

Scheme 5.1: Proposed decomposition pathway for *p*-cresol.

Through careful analysis of the 2nd derivative curve, which is presented in figure 5.2, several processes were likely to occur given the changes from linearity in the curve.

The peak max was also determined for this curve and is an alternate method of determining applicable decomposition temperature ranges.

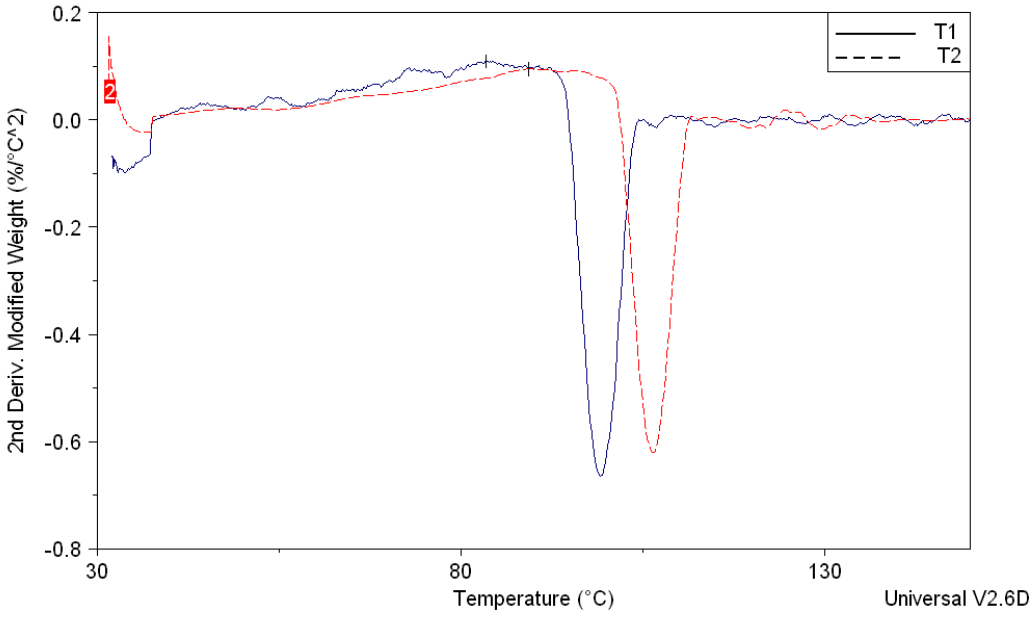

Figure 5.2: 2nd derivative curves for *p*-cresol.

From the DSC curve of *p*-cresol, in the sealed pans, the melting point and the boiling point was observed. Figure 5.3 shows two endothermic peaks with a maximum centered at 31.84 °C and 203.47 °C for a 6.960 mg sample.

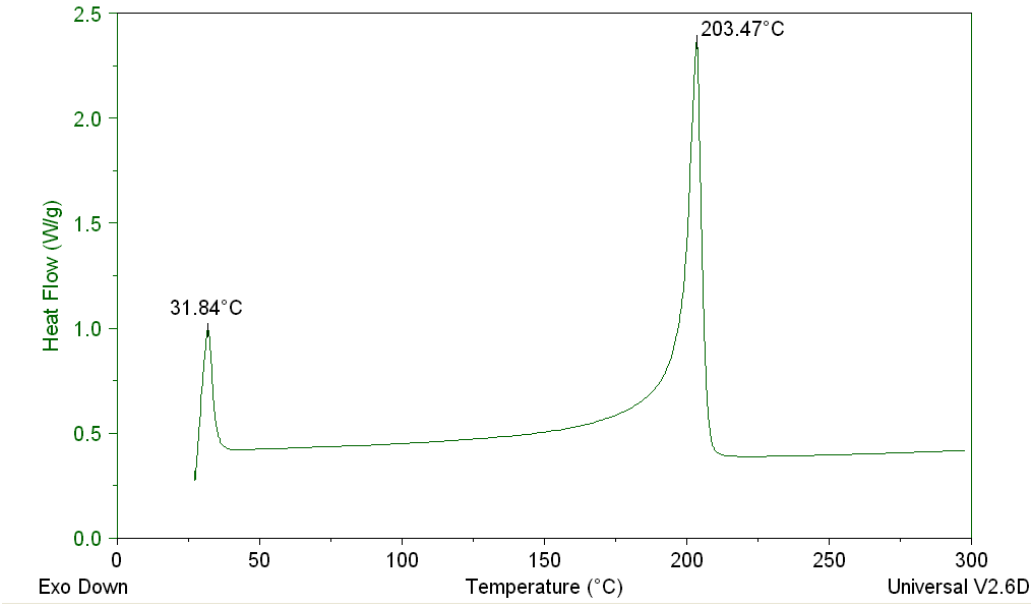

Figure 5.3: DSC curve for *p*-cresol.

Literature melting and boiling points have been reported from 33 to 34 °C and 200 to 203 °C, respectively.[21,22] The average melting point for *p*-cresol was measured at 31.84 ± 0.72 °C with a boiling point of 199.28 ± 4.19 °C. The DSC curve of *p*-cresol, in the unsealed pan, is presented in figure 5.4. This DSC curve is for a 10.655 mg *p*-cresol sample that does not contain a melting point determination but just one endothermic peak centered at 157.18 °C.

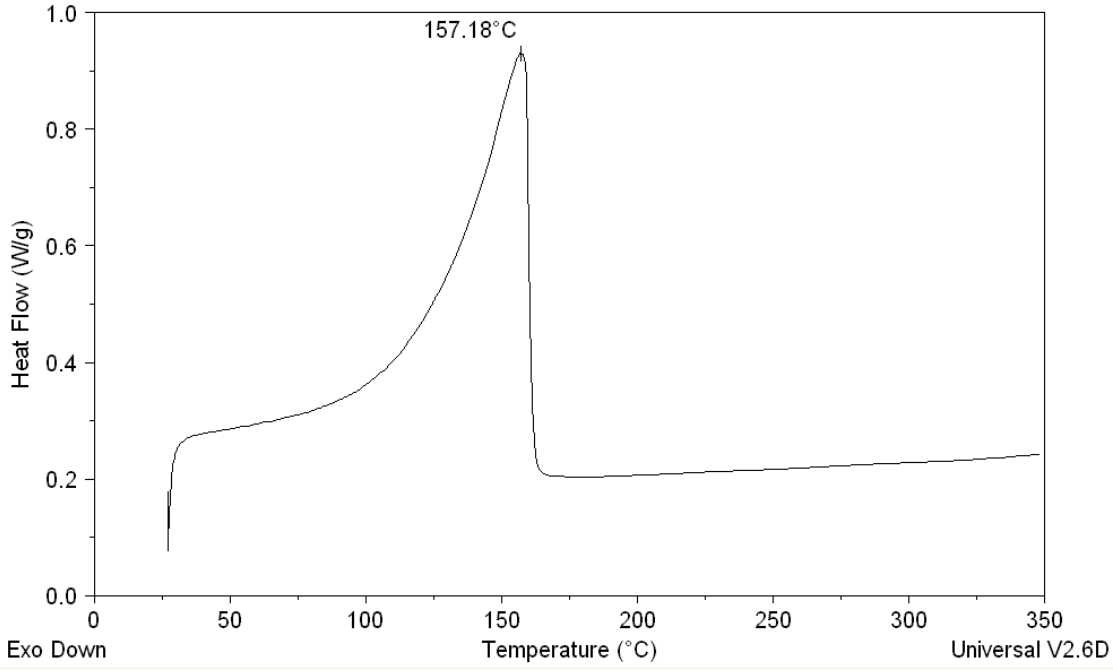

Figure 5.4: Open panned DSC curve of *p*-cresol.

5.1.2. 2-Ethylphenol

The TGA curve for 2-ethylphenol presented in figure 5.5 illustrates a single stage decomposition with mass loss occurring in three steps. Table 5.2 summarizes the observed mass percent loss over each temperature range. While the TGA curve for 2-ethylphenol might appear to be very similar to that of *p*-cresol, the measured mass percent loss is different where a combination of two degradation pathways is likely occurring.

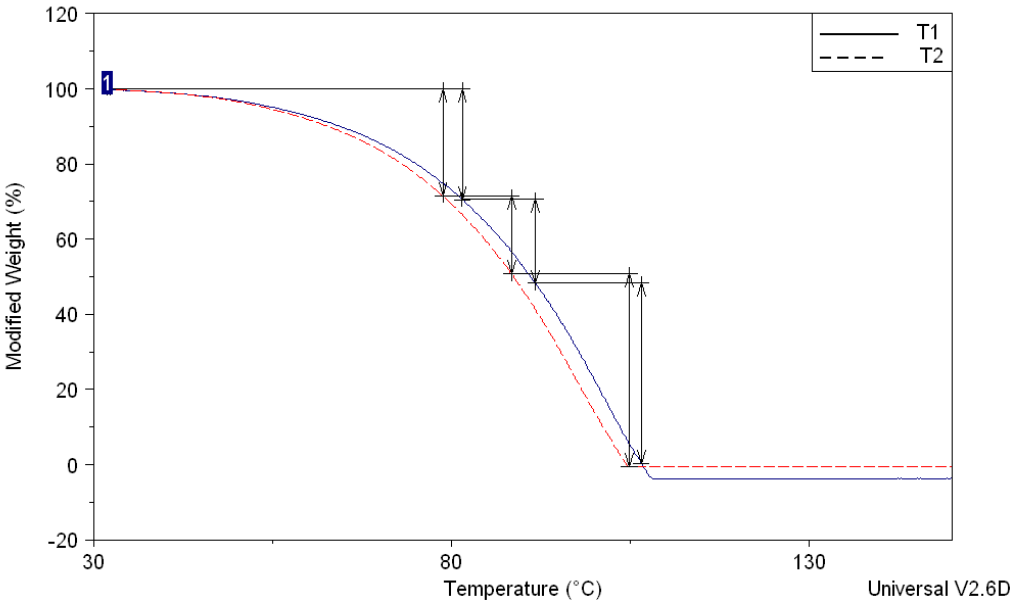

Figure 5.5: TGA curve for 2-ethylphenol.

Compound	Sample	Temperature Range	Mass % loss
2-ethylphenol	T1	32 to 82°C	29.5
		82 to 92°C	22.29
		92 to 106°C	47.84
	T2	32 to 79°C	28.54
		79 to 89°C	20.81
		89 to 104°C	49.69

Table 5.2: Onset analysis of 2-ethylphenol.

The proposed degradation pathways for 2-ethylphenol are summarized in scheme 5.2 where the top pathway includes the loss of an ethyl group (23.77 %) in the first step, followed by a loss of CO (22.95 %). The second degradation pathway involves the loss of water along with an ethyl group (38.52 %) in the first step. The second step in the bottom pathway would involve the loss of C_2H_2 which corresponds to a mass percent loss of 21.31 %. Scheme 5.2 summarizes the proposed mass loss for 2-ethylphenol.

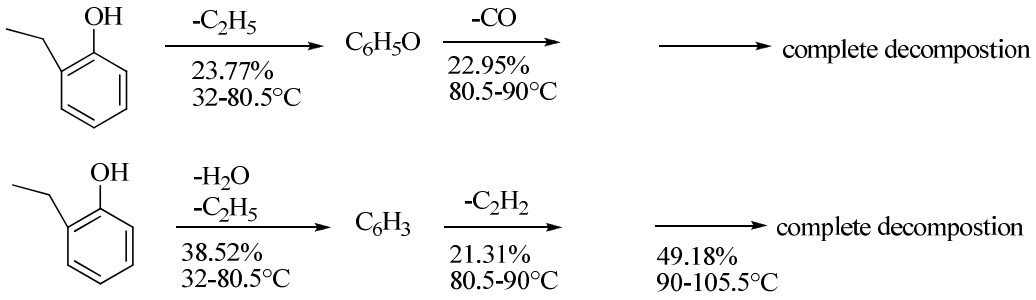

Scheme 5.2: Two proposed decomposition pathways of 2-ethylphenol.

From the DSC curve of 2-ethlyphenol in a sealed pan, the melting point was not observed due to the sample being a liquid. The observed boiling point for 2-ethylphenol was 187.16 ±1.47 °C with literature values ranging between 202 and 203 °C. [23] The open DSC of 2-ethylphenol in figure 5.6 contained one endothermic peak centered at 152.52 °C.

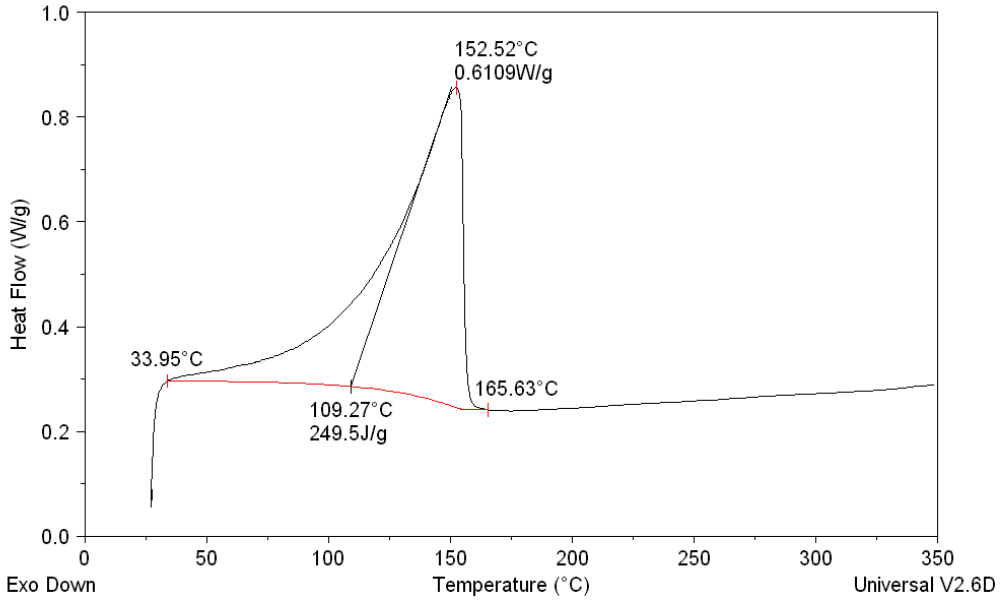

Figure 5.6: Open pan DSC curve for 2-ethylphenol.

5.1.3. 2,6-Dimethylphenol

The observed mass percent loss and temperature range from the three step single stage decomposition of 2,6-dimethylphenol is presented in Table 5.3. The measured mass percent loss for this first step from the TGA curve in Figure 5.7 is 42.66 % compared to the predicted mass percent loss of 42.62 from a loss of C_4H_4. The second decomposition step of 2,6-dimethylphenol is observed to include a mass loss of 25.74 % which would likely correspond to the predicted loss of 23.77 % from CHO. Scheme 5.3 summerizies the proposed successive mass loss for 2,6-dimethylphenol.

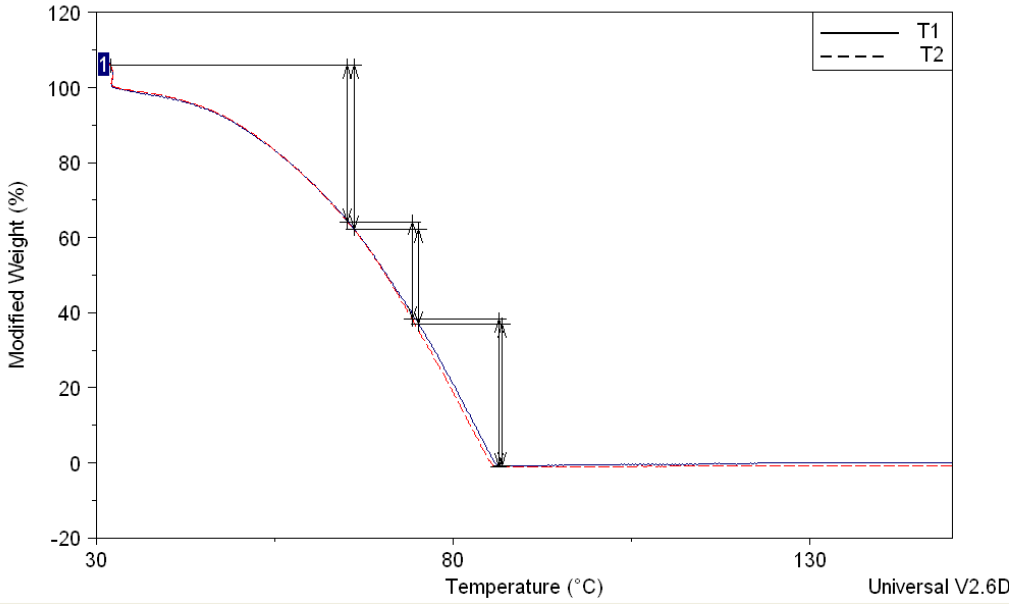

Figure 5.7: TGA curve for 2,6-dimethylphenol.

Compound	Sample	Temperature Range	Mass % loss
2,6-dimethylphenol	T1	32 to 66°C	43.61
		66 to 75°C	25.42
		75 to 85°C	37.64
	T2	32 to 65°C	41.70
		65 to 74°C	26.06
		74 to 86°C	39.35

Table 5.3: Onset analysis for 2,6-dimethylphenol.

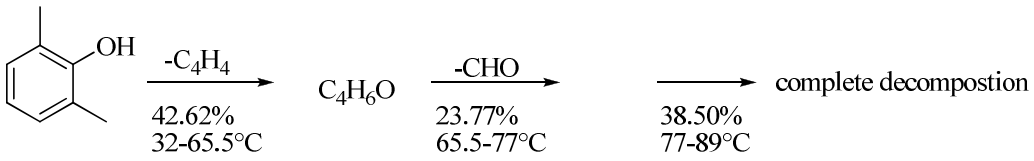

Scheme 5.3: Proposed decomposition pathway for 2,6-dimethylphenol.

The melting point for 2,6-dimethylphenol was measured at 42.79 ± 0.35 °C and agrees closely with literature. A boiling point measurement at 164.77 ± 8.00 °C, however, is inconsistent with the literature value being closer to 202 °C. The discrepancy in the boiling point is likely due to the high volatility of this compound. The melting and boiling points were determined from the DSC curve using sealed pans in figure 5.8.

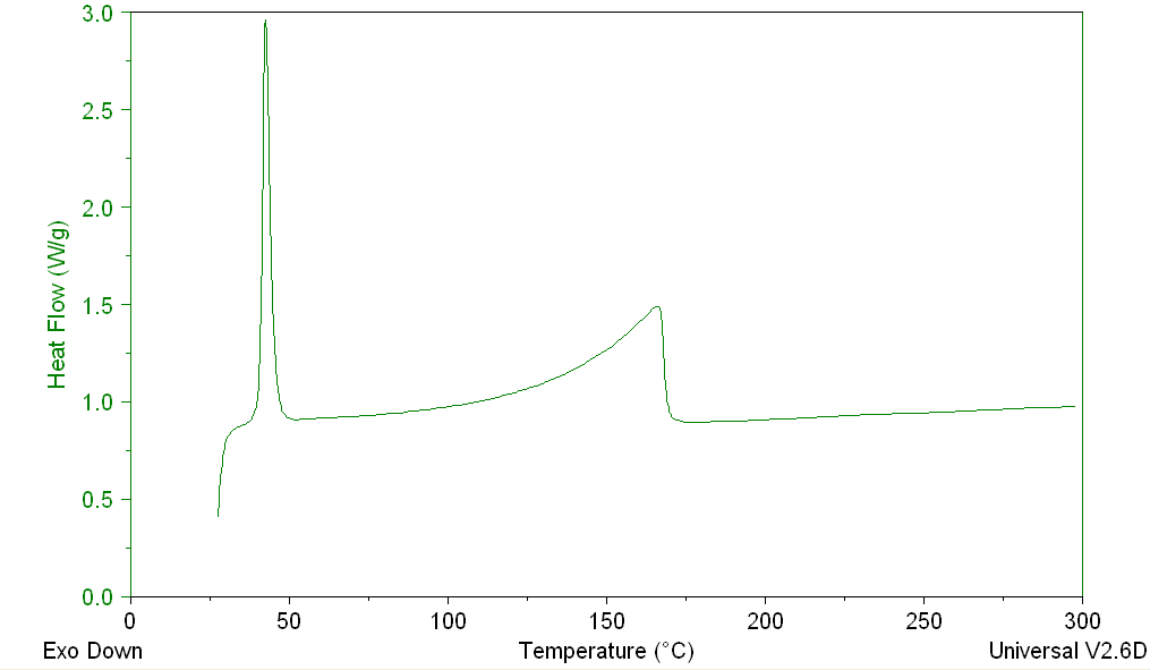

Figure 5.8: DSC of 2,6-dimethylphenol.

5.1.4. 3,5-Dimethylphenol

The observed mass percent losses corresponding to the inflection points on the TGA curve of 3,5-dimethylphenol from figure 5.9 are likely due to the loss CHO and in the first step between 32 and 88 °C. The measured mass percent loss for this first step is 23.82 % compared to the predicted mass percent loss of 23.77. The second step of the single stage decomposition of 3,5-dimethylphenol is observed to include a mass loss of 25.38 % which corresponds very closely to the predicted loss of 24.59 % from the loss of two CH_3 groups. Table 5.4 contains the temperature range and observed mass percent

losses during the three step single stage decomposition of 3,5-dimethylphenol while Scheme 5.4 illustrates the proposed thermal decomposition pathway.

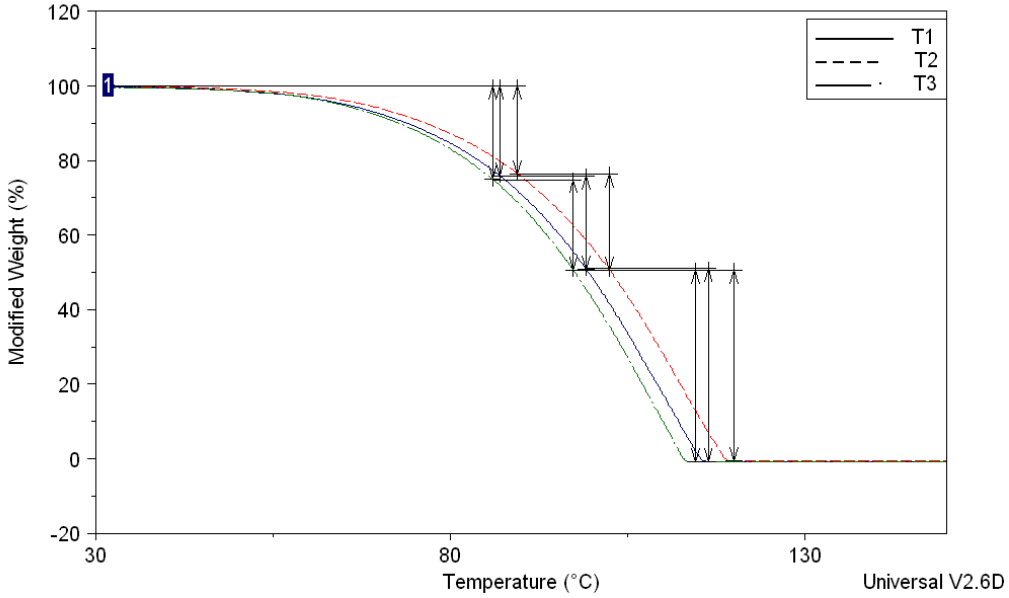

Figure 5.9: TGA curve for 3,5-dimethylphenol.

Compound	Sample	Temperature Range	Mass % loss
3,5-dimethylphenol	T1	32 to 87°C	24.06
		87 to 99°C	24.95
		99 to 116°C	51.70
	T2	32 to 90°C	23.57
		90 to 103°C	25.81
		103 to 120°C	51.07
	T3	32 to 86°C	25.10
		86 to 97°C	24.38
		97 to 115°C	51.30

Table 5.4: Onset analysis of 3,5-dimethylphenol.

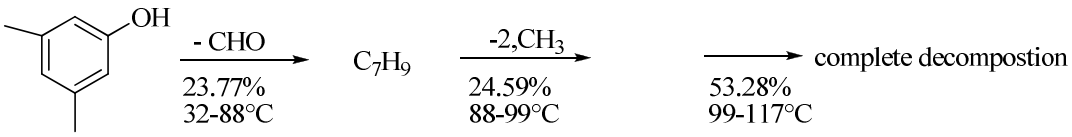

Scheme 5.4: Proposed decomposition of 3,5-dimethylphenol.

The melting point of 3,5-dimethylphenol was measured to be 63.09 ± 2.11 °C while the boiling point was 219.59 ± 3.26 °C. Literature values are 64 °C and 219 °C, respectively.[24]

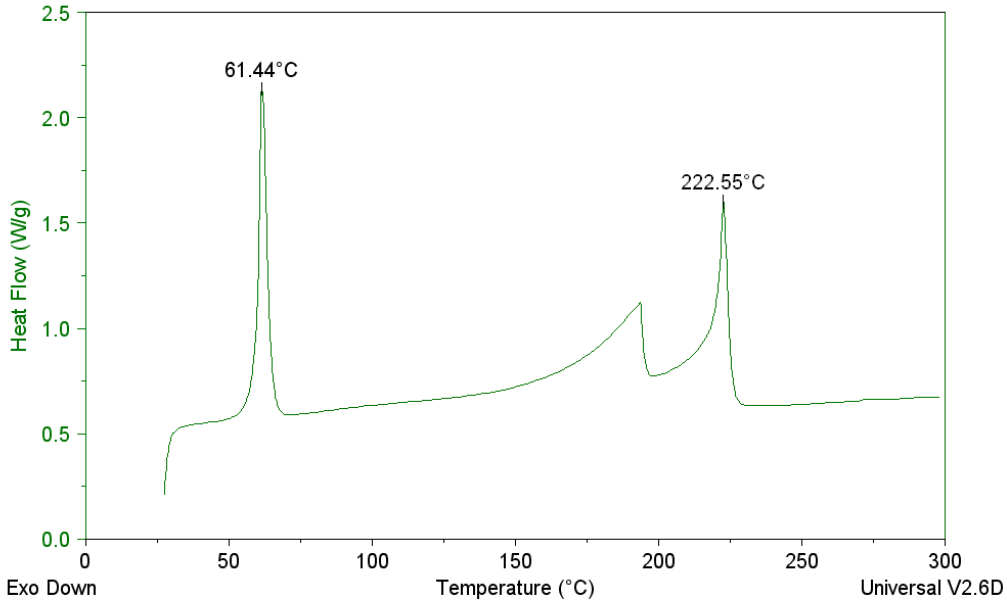

Figure 5.10: DSC curve of 3,5-diemethylphenol.

The open pan DSC curve for 3,5-dimethylphenol, shown in figure 5.11, consists of two endothermic peaks, the first corresponding to the melting of 3,5-dimethylphenol with a peak max at 62.18 °C and the other endothermic process centered at 168.57 °C.

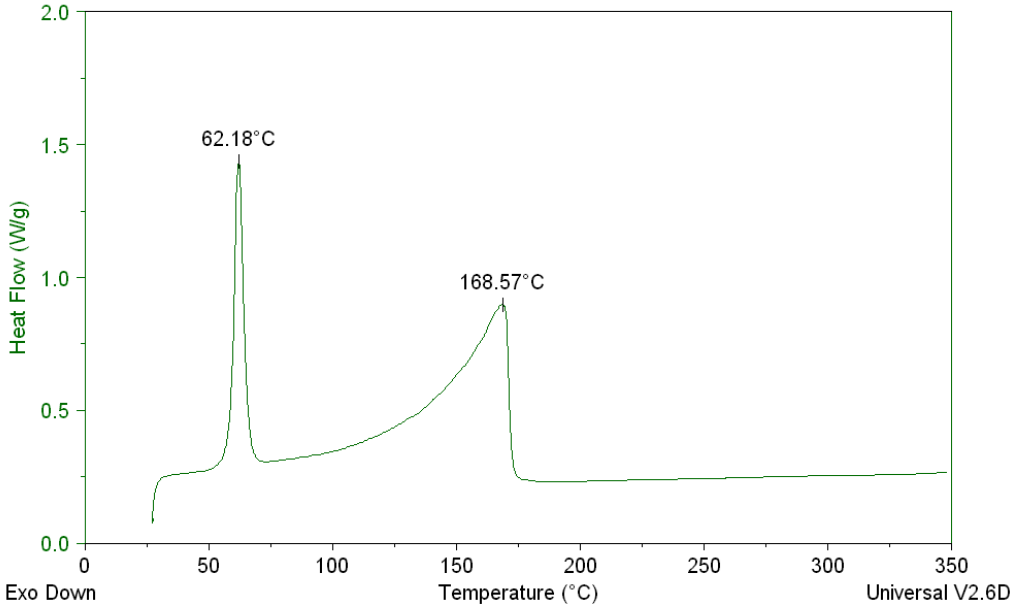

Figure 5.11: Open pan DSC curve for 3,5-dimethylphenol.

5.2. Thermal Analysis Diacetone-D-glucose and 2-phenylacetyl ester

5.2.1. Diacetone-D-Glucose

The thermal decomposition of diacetone-D-glucose, presented in figure 5.12, was analyzed in a similar fashion to previously described phenol derivatives by measuring the inflection points of the single stage TGA curve.

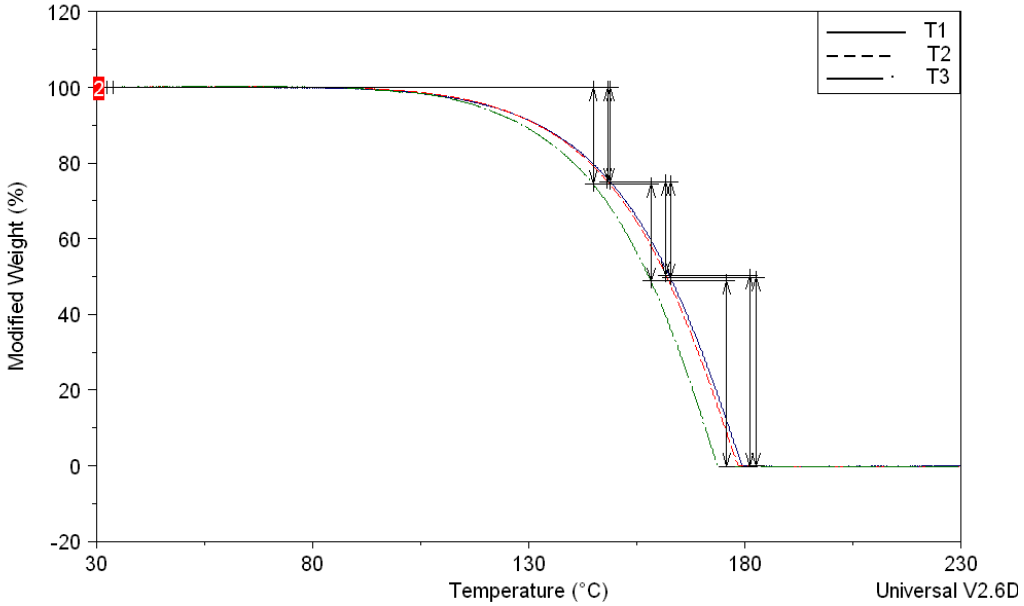

Figure 5.12: TGA curve of Diacetone-D-glucose.

The corresponding mass percent losses, presented in table 5.5, is likely the loss of both C_3H_4 and CO group in two successive steps which corresponds to calculated mass percent loss of 26.15%.

Compound	Sample	Temperature Range	Mass % loss
Diacetone-D-glucose	T1	34 to 149°C	25.02
		149 to 163°C	25.3
		163 to 183°C	49.77
	T2	32 to 148°C	24.92
		148 to 162°C	24.82
		162 to 181°C	50.44
	T3	32 to 145°C	25.57
		145 to 158°C	25.63
		158 to 176°C	49.12

Table 5.5: Onset analyses of Diacetone-D-glucose.

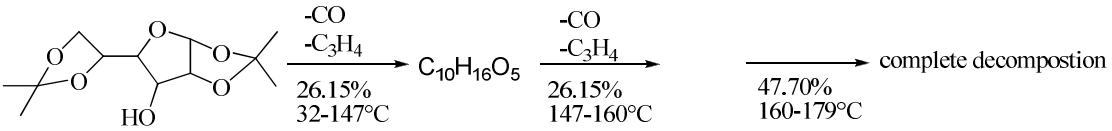

Scheme 5.5: Proposed decomposition of Diacetone-D-glucose.

The DSC of diacetone-D-glucose presented in figure 5.13, shows two endothermic peaks centered at 107.95 °C and 245.09 °C. The first peak corresponds to the reported melting point for the compound between a 108 and 110 °C. There is also some deviation from linearity before the second endothermic peak where the molecule is likely further decomposing or undergoing dehydration processes.

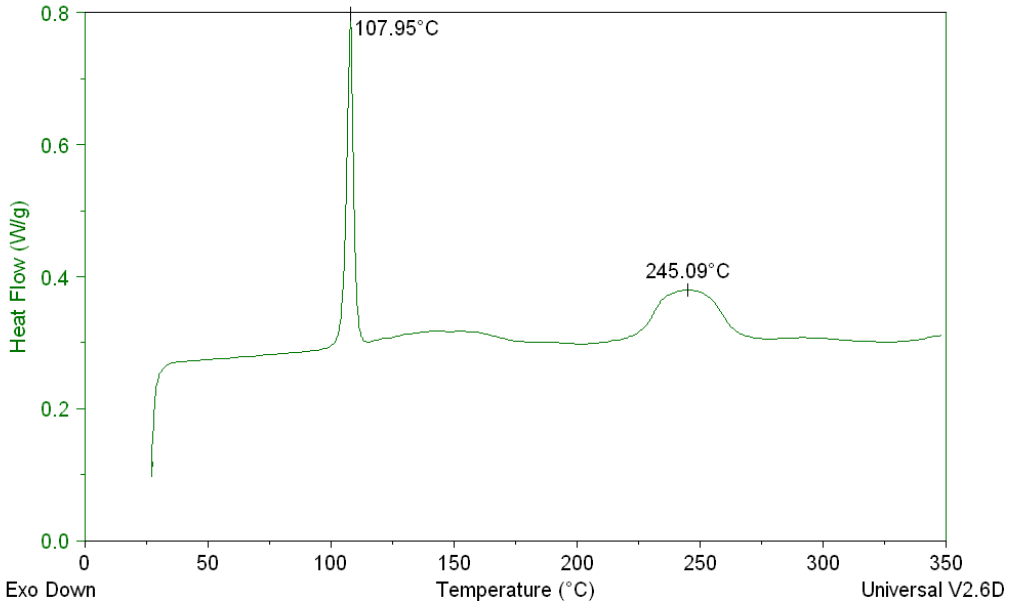

Figure 5.13: DSC curve of Diacetone-D-glucose.

The DSC curve in figure 5.14 is the open pan DSC curve for diacetone-D-glucose. The DSC curve also shows two endothermic peaks centered at 108.49 °C and 194.48 °C.

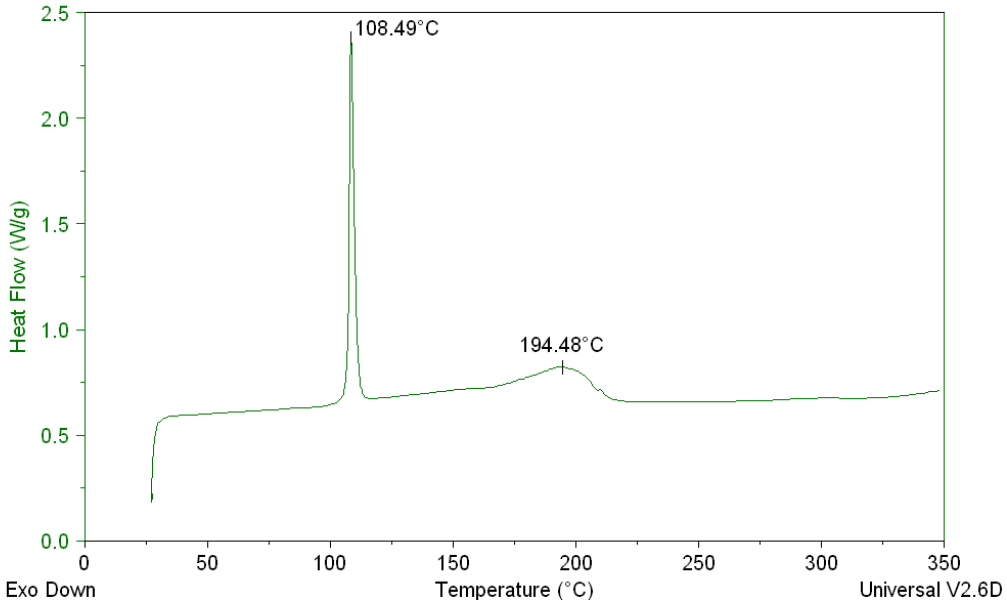

Figure 5.14: Open pan DSC curve of Diacetone-D-glucose.

5.2.2. 2-Phenylacetyl ester

The TGA curve for 2-phenylacetyl ester, presented in figure 5.15, shows a mass loss occurring over three steps between the average range of 32 and 201 °C for the first step, 201 and 216 °C for the second step, and 216 and 236 °C for the final step. Table 5.6 summarizes the observed mass percent losses for 2-phenylacetyl ester.

Compound	Sample	Temperature Range	Mass % loss
2-phenylacetyl ester	T1	32 to 204°C	25.06
		204 to 219°C	24.72
		219 to 240°C	50.38
	T2	32 to 196°C	25.71
		196 to 210°C	24.67
		210 to 229°C	24.72

Table 5.6: Onset analysis of 2-phenylacetyl ester.

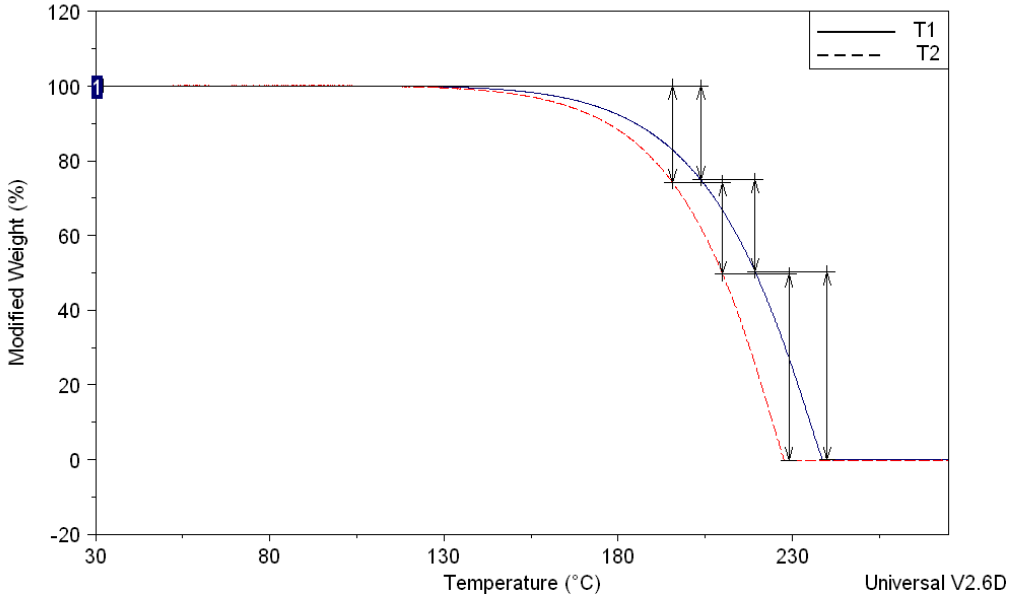

Figure 5.15: TGA curve of 2-phenylacetyl ester.

The observed mass losses correspond to a loss of CHO and C_5H_6 (25.13 %) for the first step, a loss of C_6H_6 and CH_3 yielding mass percent loss of 24.60 % in the second step.

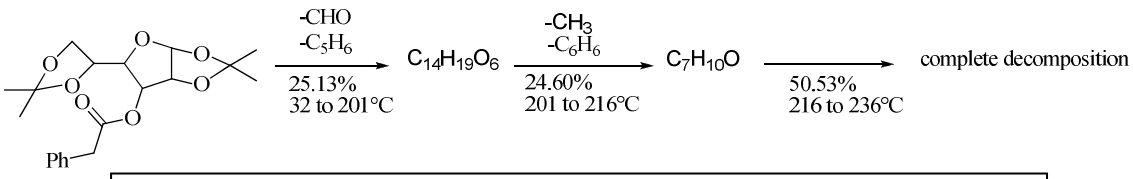

Scheme 5.6: Proposed decomposition pathway for 2-phenylacetyl ester.

The DSC curve for 2-phenylacetyl ester, presented in figure 5.16, shows a sharp endothermic peak centered at 68.90 °C. The average peak max for this process was 69.22 ± 0.30 °C and corresponds to the melting point. There is also a broad exothermic peak centered at 219.77, which is likely oxidation, followed by degradation.

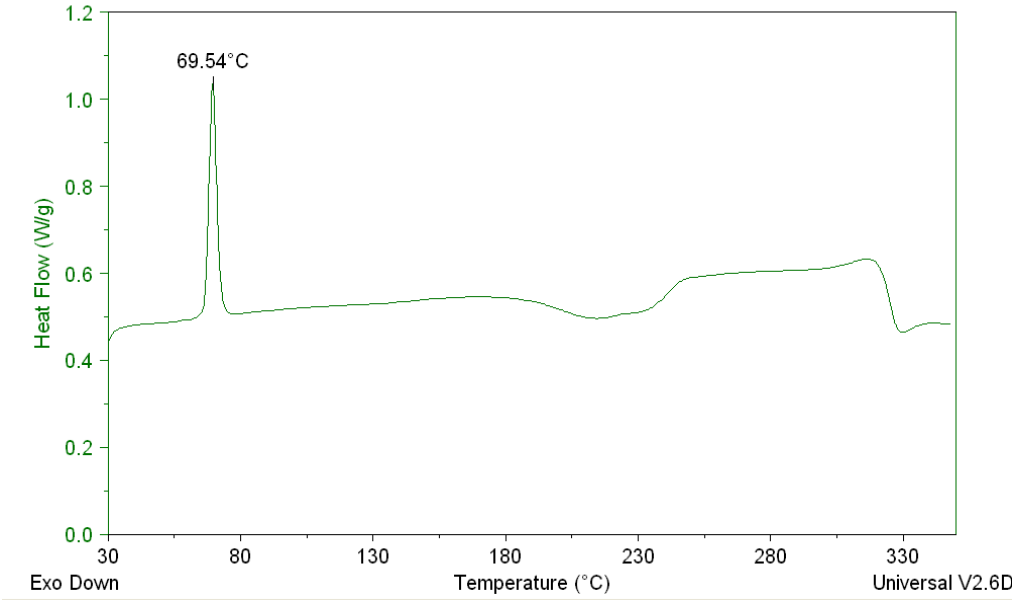

Figure 5.16: DSC curve of 2-phenylacetyl ester.

The open pan DSC curve for 2-phenylacetyl ester, presented in figure 5.17, shows the melting process centered at 68.81 °C. An exothermic peak is also observed, but the intensity of the peak has decreased. The broad endothermic peak in this figure further supports the closed pan DSC result where the molecule is undergoing decomposition.

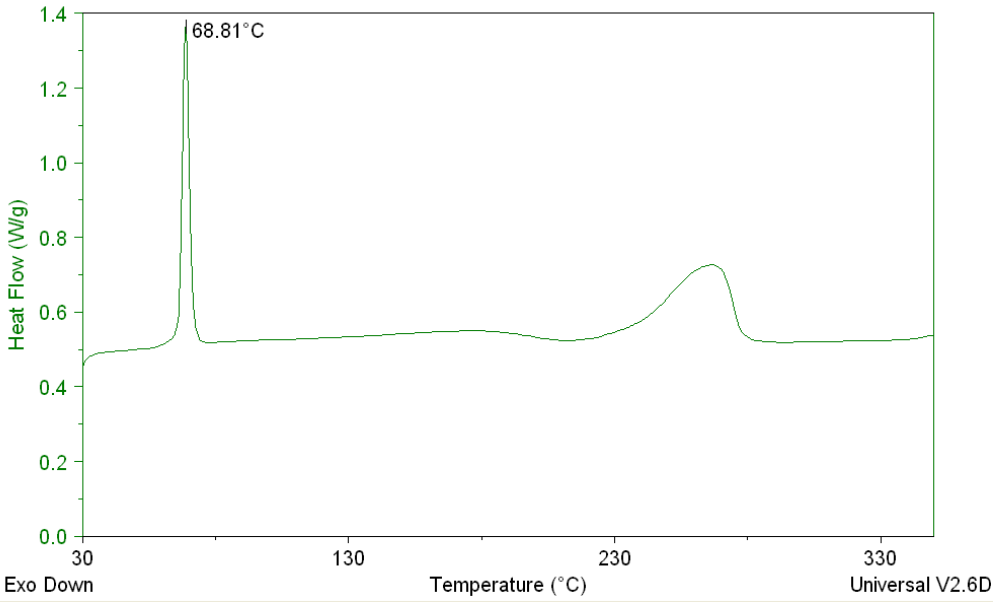

Figure 5.17: Open pan DSC curve of 2-phenylacetyl ester.

6. Comparison of MS and TA

6.1. Phenol Derivatives

6.1.1. *p*-Cresol

From the mass spectrum of *p*-cresol, the molecular ion was the most intense peak, illustrating the overall stability of the molecule. The [M-H] peak at m/z 107, with a relative intensity of 76.39%, is the second most intense peak and is due to hydrogen loss from the benzene ring. The loss of water is observed in the mass spectrum at m/z 89 with a relative intensity of 4.37% as is the loss of CO at m/z 79 with a relative intensity of 4.37%. From the mass spectrum, the loss of oxygen-containing fragments is a very common pathway, second to the loss of hydrogen, and occurs before the loss of any alkyl group. The principle fragmentation pathway is for *p*-cresol illustrated in figure 6.1.

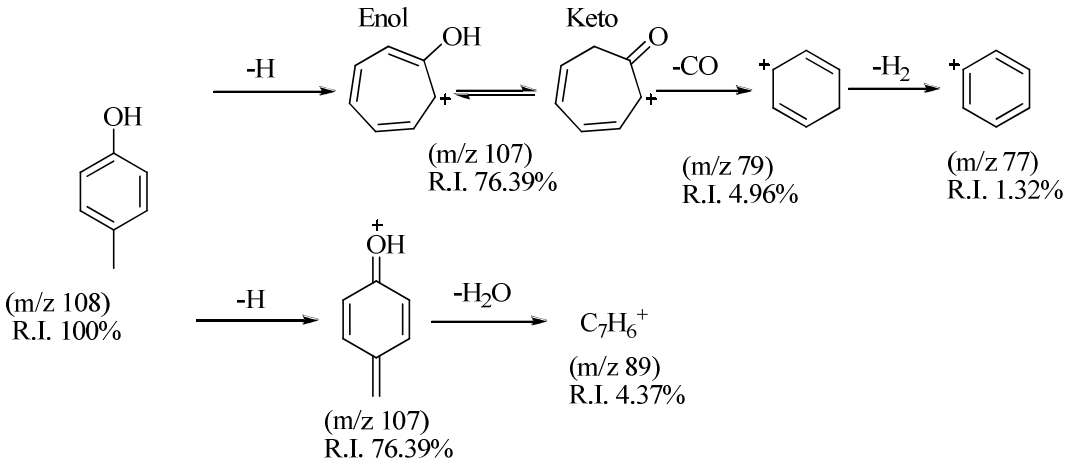

Figure 6.1: Principle fragmentation pathway for *p*-cersol.

From the proposed decomposition pathway for *p*-cresol, presented in figure 6.2, single stage decomposition occurring from 32 to 102 °C is observed. The DSC curve for *p*-

cresol shows the molecule decomposing shortly after melting. From the analysis of the TGA curve, a three step mass percent loss was observed. The first step mass percent loss average for *p*-cresol is 31.80%, which corresponds to the loss of a methyl group and H_2O. Since the molecule is not inhibited in any way with a methyl group being *meta* or *ortho* to the hydroxyl group, the molecule can readily lose an OH group along with a hydrogen and then a CH_3 group. The proposed mass percent loss for this step is 30.56%, compared to the observed value of 31.80%. This trend agrees with MS data in that oxygen-containing specie came off in the first step. The second step corresponds to the loss of C_2H_2 with a calculated mass percent loss of 24.07%. The mass percent loss average for the second step was 24.37%. Finally the molecule is completely decomposed between 90 to 102 °C.

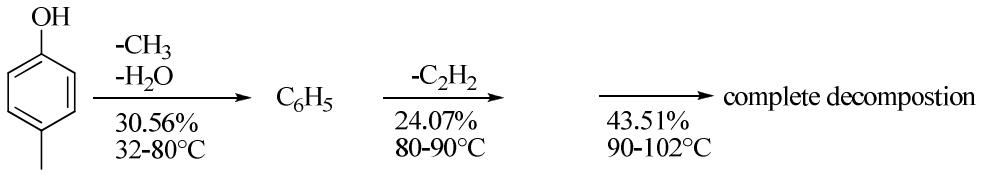

Figure 6.2: Proposed decomposition pathway for *p*-cresol.

6.1.2. 2-Ethylphenol

The most intense peak observed for 2-ethylphenol was the [M-CH_3] peak with a relative intensity of 100%. The second most intense peak observed was the molecular ion peak with a relative intensity of 69.02%. The peak at m/z 91 is more intense than the fragment seen in the mass spectrum for *p*-cresol with a relative intensity of 11.8 5%. The peaks at m/z 79 and 77 have relative intensities of 36.97% and 32.87%, respectively. From the MS data, a loss of a carbon-containing species, followed by a loss of an

oxygen-containing species is expected. The principle fragmentation pathway for 2-ethylphenol is illustrated in figure 6.3.

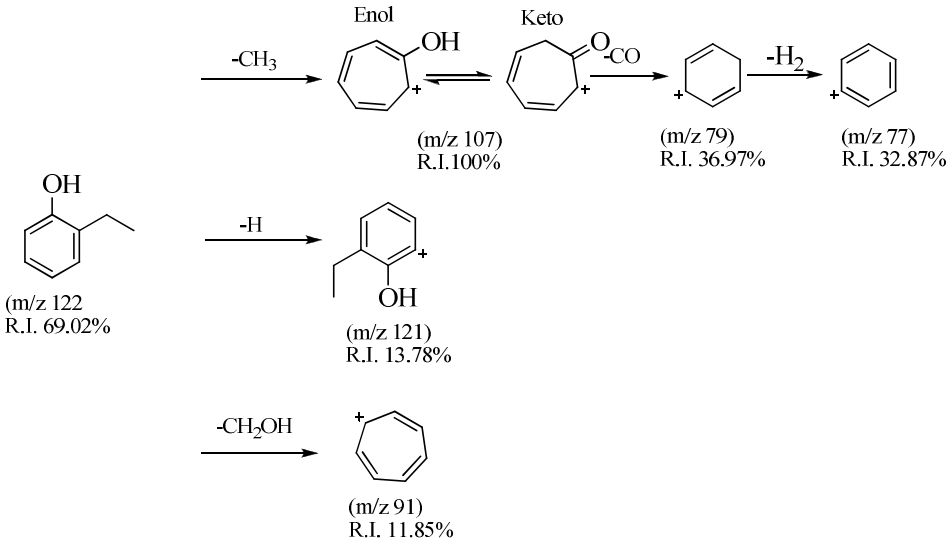

Figure 6.3: Principle fragmentation pathway for 2-ethylphenol.

The TGA curve of 2-ethylphenol showed a single stage decomposition occurring between 32 and 106 °C. From the mass spectrum, there are intense peaks consistent with the loss of the oxygen-containing fragment and the loss of the methyl radical suggesting that these bonds are the preferred bond rupture location. The DSC curve for 2-ethylphenol did not show melting because the sample is a liquid, but it did show that the molecule is decomposing at 33.95 °C. The proposed thermal degradation occurred in three steps, where the first step involved the loss of an ethyl group or the loss an ethyl group and water. There are two suggested schemes for this molecule because the molecule has an ethyl group and a hydrogen atom *ortho* to the hydroxyl group. The mass percent loss for the first step for both proposed pathways are 22.37% and 38.52%. If both processes were occurring equally at same time, the average mass percent loss for the first step is 30.45

which is close to the observed average mass percent loss of 29.02%. The second step of the decomposition corresponds to the loss of either CO in the first scheme or C_2H_2 in the second scheme. The mass percent loss for the first scheme is 22.95% and for the second scheme it is 21.31%, giving an average of 22.13. The observed average mass percent loss for the second step in the single stage decomposition of 2-ethylphenol is 21.55 °C, slightly below room temprature. The molecule then completely decomposes between 90 to 106 °C. Figure 6.4 illustrates the proposed thermal decomposition.

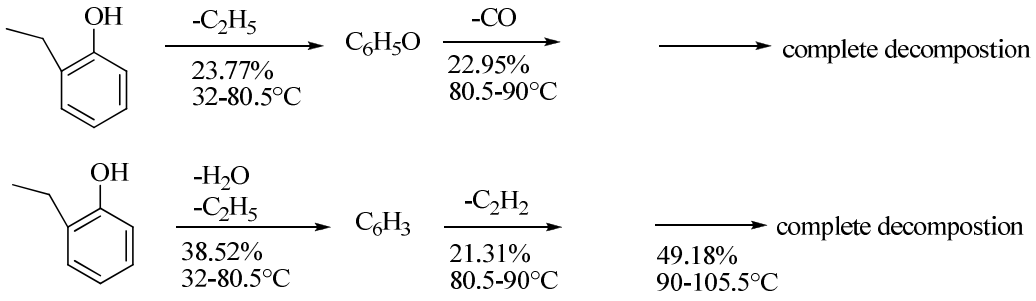

Figure 6.4: Two proposed decomposition pathways for 2-ethylphenol.

6.1.3. 2,6-Dimethylphenol

For 2,6-dimethylphenol, the most intense peak is the molecular ion peak. The peak at m/z 107, due to the loss of a methyl radical, has a relative intensity of 73.06%. The [M-H] peak has relative intensity of 28.5%. The peak at m/z 91 has a relative intensity of 29.55% compared to the relative intensity of *p*-cresol and 2-ethylphenol at 0.94% and 11.85%, respectively, for a similar fragmentation pathway. The peaks at m/z 79 and 77 have relative intensities of 19.79% and 21.02%, respectively. Generally, the fragments observed in the mass spectrum of 2,6-dimethylphenol are more intense than the fragments observed in the other three phenol derivatives, suggesting this molecule is

easy to fragment. From the mass spectrum, the principle fragmentation pathway follows the loss of a methyl radical and the loss of a CH_2OH group from the molecular ion. The principle fragmentation pathway is presented in figure 6.5. Species that have lost oxygen-containing fragments have the highest intensities, meaning that this type of fragmentation pathway is preferred.

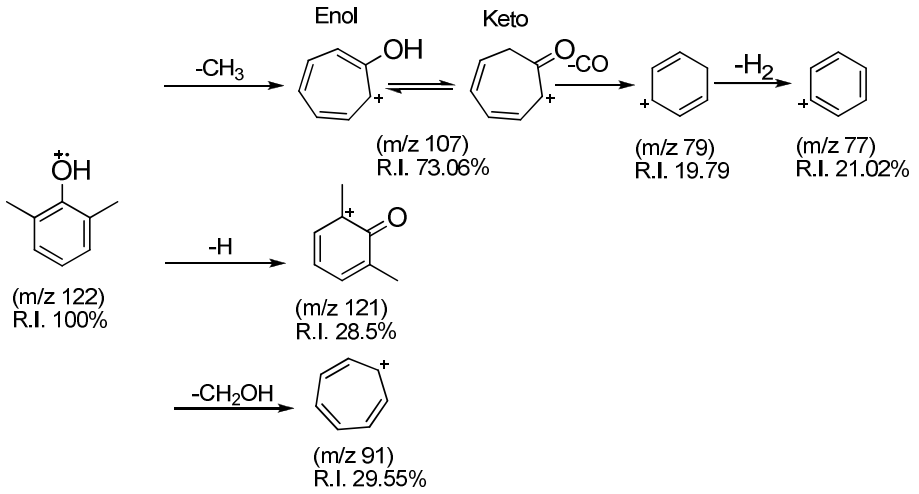

Figure 6.5: Principle fragmentation pathway of 2,6-dimethylphenol.

This compound also provided a single stage decomposition TGA curve. The decomposition of 2,6-dimethylphenol occurred between 32 and 89 °C, giving a more narrow range than the other two compounds previously discussed, supporting the mass spectrum in that the molecule is easily destroyed. The DSC curve of 2,6-diemthylphenol shows melting followed by the onset of decomposition shortly after. The single stage curve provided a three step mass percent loss for the decomposition of 2,6-dimethylphenol. The first step corresponds to the loss of C_4H_4 with a calculated mass percent loss of 42.62%. The loss of C_4H_4 agrees with the MS data, showing a loss of carbon-containing specie first. This loss is also preferred because there is a methyl group

in both ortho positions relative to the hydroxyl group preventing the loss of the oxygen-containing specie. The observed average mass percent loss for the first step is 42.66%. The second step involves the loss of a CHO group with calculated mass percent of 23.77% compared to the measured mass percent loss average of 25.74%. The molecule then goes on to completely decompose between 77 and 89 °C as illustrated in figure 6.6.

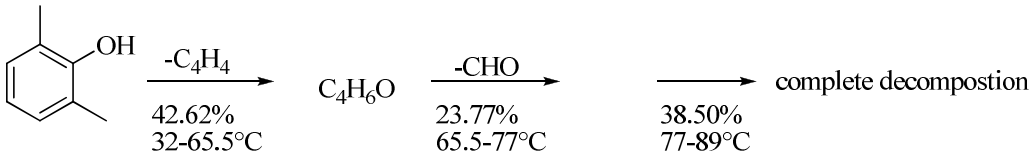

Figure 6.6: Proposed decomposition pathway for 2,6-dimethylphenol.

6.1.4. 3,5-Dimethylphenol

As in the case of 2,6-dimethylphenol, the molecular ion of 3,5-dimethylphenol is the most intense peak. The [M-CH_3] peak has a relative intensity of 33.52%, while the [M-H] peak has a relative intensity of 20.58%. The peak at m/z 91 has a relative intensity of 2.26%, which is less then 2,6-dimethylphenol and 2-ethylphenol but higher than *p*-cresol. The peaks at m/z 79 and 77 have relative intensities of 2.84% and 0.89, respectively. The relative intensity of these fragments, presented in figure 6.7, are the lowest for this compound suggesting that this compound is more stable in a highly energized environment. The MS data supports the loss of carbon-containing specie followed by the loss of oxygen-containing species.

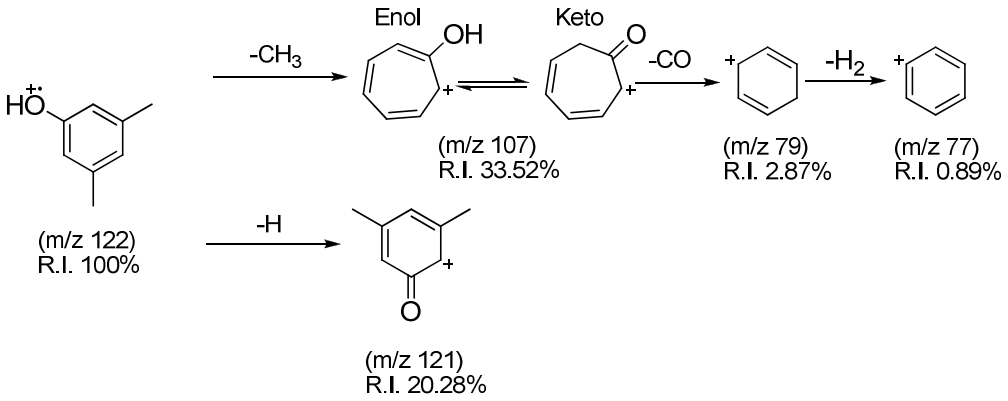

Figure 6.7: Principle fragmentation pathway for 3,5-dimethylphenol.

The DSC curve for 3,5-dimethylphenol illustrates melting and then the onset of the decomposition. The TGA curve for 3,5-dimethylpehnol shows a single stage decomposition occurring between 32 and 117 °C, suggesting that this compound is more stable than other phenol derivatives investigated. From the analysis of the TGA curve, a three step decomposition pathway was calculated and is presented in figure 6.8. The first step corresponds to a loss of oxygen-containing specie as a CHO group with a calculated mass percent loss of 23.77%. In this molecule there is no methyl group inhibiting the loss of the oxygen-containing specie, so the oxygen-containing specie is lost first. The MS data is not consistent with the TA data since we observed the oxygen-containing specie leaving in the first step. The observed average mass percent loss for the first step was 24.24%. The second step involves the loss of two CH_3 groups corresponding to a mass percent loss of 24.59% compared to the average observed mass percent loss of 24.3%. The sample completely decomposes between 99 and 117 °C.

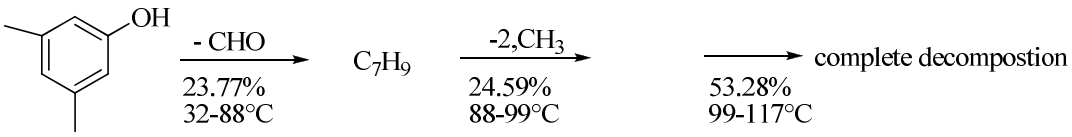

Figure 6.8: Proposed decomposition pathway of 3,5-dimethylphenol.

6.2. Diacetone-D-Glucose and 2-Phenylacetyl Ester

6.2.1. Diacetone-D-Glucose

In the mass spectrum of diacetone-D-glucose, the most intense peak is the $[(M-C_3H_4)(M)+Na]^+$ peak, which occurs upon ionization. The principle fragmentation pathway observed, presented in figure 6.9, was through a loss of C_3H_4 from the molecular ion and the $[(M-C_3H_4)(M)+Na)]^+$ peak.

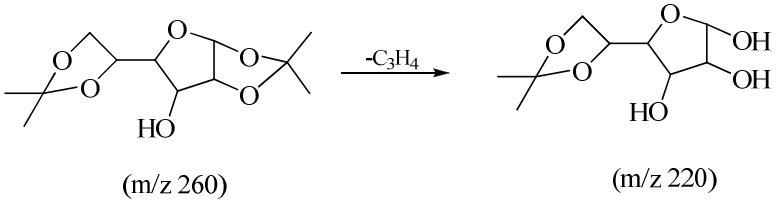

(m/z 260) (m/z 220)

Figure 6.9: Principle fragmentation pathway for Diacetone-D-glucose.

The DSC curve for this compound showed melting and then a broad endothermic peak in-between melting and boiling which is indicative of decomposition. The compound underwent single stage decomposition from the TGA curve occurring from 32 to 179 °C, depending on the mass. Through the analysis of the TGA curve, similar to that of the phenol derivatives, a three step decomposition pathway for diacetone-D-glucose was calculated. The first and second steps correspond to the consecutive loss of both C_3H_4 and CO, corresponding to a calculated mass percent loss of 26.15%. Figure 6.10

illustrates the proposed thermal decomposition for diacetone-D-glucose. The observed average mass percent loss for the first step was 25.17% and 25.25% for the second step with complete decomposition following.

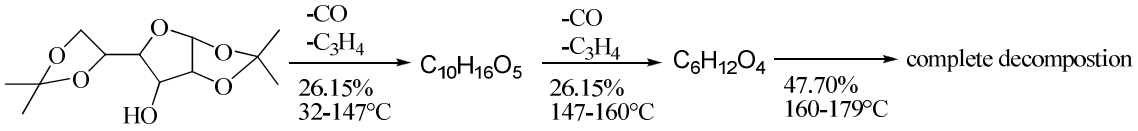

Figure 6.10: Proposed decomposition pathway of Diacetone-D-glucose.

6.2.2. 2-Phenylacetyl Ester

In the mass spectrum of the 2-phenyacetyl ester, the most intense peak is the molecular ion peak with the addition of sodium, $[M+Na]^+$. The principle fragmentation pathway, presented in figure 6.11, observed in this compound occurs through the loss of C_3H_5O successively yielding peaks at m/z 321 and 263. A peak at m/z 91 is also observed for the mass spectrum of the 2-phenylacetyl ester.

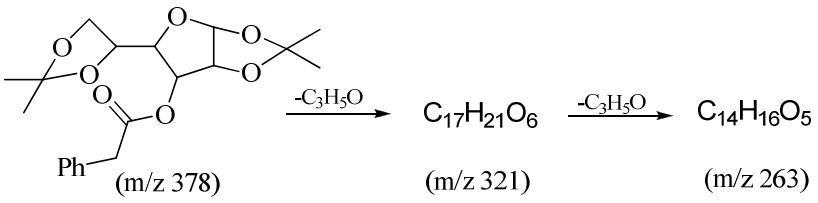

Figure 6.11: Principle fragmentation pathway for 2-phenylacetyl ester.

The DSC curve for the 2-phenylacetyl ester showed a melting peak, a broad exothermic peak where oxidation is taking place, and then a final endothermic peak. The DSC curve supports that the molecule is decomposing in the range investigated by TGA. The TGA

curve of the 2-phenylacetyl ester showed a single stage decomposition occurring in three steps between 32 and 236 °C. (Figure 6.12) The first step corresponds to the loss of CHO and C_5H_6 with a calculated mass percent loss of 25.13% compared to the observed mass percent loss of 25.39%. The MS data supports this loss as the observed principle fragmentation pathway supports the loss of both oxygen and carbon. The second loss is consistent with the loss of a benzene ring and CH_3 with a calculated mass percent loss of 24.60%. The observed average mass percent loss for 2-phenylacetyl ester in the second step was 24.70%. The final stage involves the complete decomposition of the 2-phenylacetyl ester.

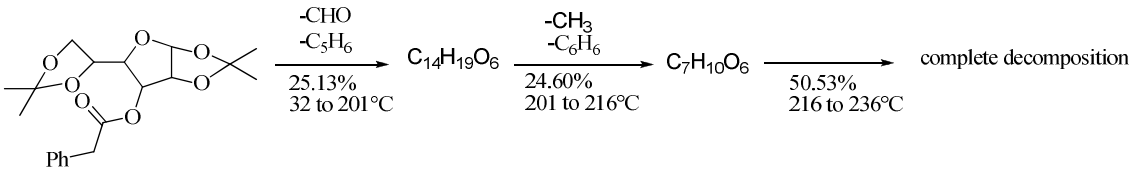

Figure 6.12: Proposed decomposition pathway for 2-phenylacetyl ester.

7. Discussion

7.1. Mass spectrometric behavior of phenol derivatives

The mass spectrum for all the phenol derivatives, except 2-ethylphenol, showed an intense molecular ion peak as the base peak. The base peak for 2-ethylphenol was the [M – CH_3] peak observed at m/z 107. For all the phenolic compounds investigated, the loss of methyl radical showed a significant relative intensity suggesting these compounds prefer to lose methyl radical to generate the hydroxytropylium ion.

The peak at m/z 91, which is direct evidence for the loss of alkyl group, is common to all the phenol derivatives but with varying relative intensity. 2,6-Dimethylphenol has the highest intensity, suggesting the alkyl group being *ortho* to hydroxyl group direct the loss of an alkyl group. 2-Ethylphenol also supports this finding being that it has the second largest relative intensity for the appearance of the peak m/z 91. For 3,5-dimethylphenol and *p*-cresol, however, the relative intensity for the peak at m/z is less than 1%, suggesting some alternate pathway was in effect.

The *para* effect was also observed in the mass spectrum of *p*-cresol, which allows for the loss of water. The *ortho* effect was observed in the mass spectrum of 2-ethylphenol and 2,6-dimethylphenol allowing the loss of water through secondary fragmentation of the [M – CH_3] and [M – H] fragment. The peak at m/z 89 and m/z 103 did not appear in the mass spectrum for 3,5-dimethylphenol. The peaks at m/z 79 occur through the loss of CO which is characteristic of phenol-like compounds, but instead of seeing the accompanying loss of CHO, we observed a loss of molecular hydrogen. The

relative intensity of peaks at m/z 79 and 77 are highest for 2,6-dimethylphenol and 2-ethylphenol suggesting that the placement of an alkyl group in the *meta* or *para* position can influence and even inhibit formation of these fragments. The relative intensity for 3,5-dimethylphenol and *p*-cresol was observed to be less than 5%. Similar to the trend, the peaks at m/z 65 and 63 are the most intense for the *ortho* substituted phenols and less for the *meta* and *para* substituted phenols.

7.2. Mass spectrometric behavior of Diacetone-D-glucose and 2-phenylacetyl ester

In the mass spectrum of diacetone-D-glucose and the 2-phenylacetyl ester, both compounds ionized with sodium present. We observed two different fragmentation pathways for the two carbohydrates. In the first example, diacetone-D-glucose, the molecular ion peak and the loss of C_3H_4 was observed. For the 2-phenylactyl ester, the molecular ion peak along with molecular ion dimer with sodium is observed. Upon addition of the ester, the MS fragmentation pathway changed for the molecule. The 2-phenylacetyl ester showed a loss of C_3H_5O along with the presence of the tropylium ion, which is not observed in the MS for diacetone-D-glucose. Both species showed gas phase interactions as indicated by the presence of the dimer.

7.3. Thermal behavior of phenol derivatives

The thermal behavior for the phenol derivatives were observed to be very similar to each other, where a single stage decomposition curve for all the compounds was determine. Through a more in-depth analysis, the mass percent loss for all the compounds were calculated. Independent of the mass percent loss analysis decompositions ranges,

melting and boiling points, were measured for all the compounds. From the TGA curve, we can investigate the thermal stability of the compounds. In the case of 3,5-dimethylphenol, for example, its thermal behavior exhibited stability, while 2,6-dimethylphenol readily decomposed. Interestingly in MS, 2,6-dimethylphenol gives the most intense fragments for the observed fragmentation pathway and 3,5-dimethylphenol gives the least intense fragments. There is some correlation between the thermal stability of these compounds and the relative intensity of MS data. The TGA curve for all the compounds can serve as a fingerprint for all the compounds investigated.

The DSC curves for the phenols derivatives are very different, due to the difference in melting and boiling points for the compounds. For all the samples studied, except 2-ethylphenol, the melting points of the samples were determined in close agreement with the literature values. The boiling point for most of the compounds agreed with the literature values, but the boiling point for 2,6-dimethylphenol did not. This discrepancy is likely due to the increased volatility of 2,6-dimethylphenol compared to the other phenol derivatives. The discrepancy in the reported melting and boiling points can be from the other samples having trace impurities. The open-panned DSC of the compounds was included to achieve a better comparison between TGA data. For all the open-panned DSC experiments, except *p*-cresol, the melting point was observed as was a shift in the second endothermic peak which can be assigned to the sample boiling. The shift is caused by the sample being open to the environment, thus lowering the pressure in the unsealed pan.

7.4. Thermal behavior of Diacetone-D-glucose and 2-phenylacetyl ester

From the TGA curves of diacetone-D-glucose and 2-phenylacetyl ester, the addition of ester to the furanose platform was observed to increase the thermal stability of this compound. The decomposition ranges were reported for both samples. From the DSC, the melting points were observed for both compounds. The melting points between the two compounds were observed to decrease upon the addition of the ester. The DSC curve for both compounds was observed to be unique. The DSC curve of diacetone-D-glucose shows three endothermic peaks and the DSC curve for 2-phenylacetyl ester show two endothermic peaks and an exothermic peak. These finding support the use of TA as a fingerprint when characterizing a molecule.

7.5 Conclusion

The fragmentation and thermal decomposition mechanisms for series of phenol analogs were investigated. The effects of having alkyl groups *meta*, *para*, and *ortho* to the hydroxyl group is presented. Through different pathways, we observed the breaking of weak bonds. The mass spectrum provided similar fragmentation pathways for all the phenolic analogs with varying relative intensity. The formation of certain ions and the relative intensity was observed based of the position of the alkyl substituent. From the TA data, we were able to observe the decomposition, melting, and boiling for the series of phenol analogs. All the phenol analogs provided distinct TGA and DSC data that illuminated the thermal stability of the compounds.

For the carbohydrates, the fragmentation and thermal decomposition mechanism are presented. From the mass spectrum, we observed fragmentation that is significantly different from the ester derivative. The thermal data also provided unique curves for the two carbohydrate structures that support the characterization of these particular compounds. In both cases, the data obtained from MS and TA can be used as a fingerprint in the characterization of these compounds investigated.

References

1. Fahmey, M.A.; Zayed, M.A.; *J. Therm. Anal. Calorim*. **2002**, *67*, 163-165.
2. Fahmey, M.A.; Zayed, M.A.; Keshk, Y.H.; *Thermochim. Acta*. **2001**, *366*, 183-188.
3. Barker, James. *Mass Spectrometry*, 2nd, John Wiley & Sons: Chichester, England, **1999**.
4. Downard, K., *Mass Spectrometry: A Foundation Course*, The Royal Chemistry Society, Cambridge, **2004**.
5. Haines, P.J., Thermal method of analysis. In *Environmental analytical chemistry*, 2nd, Fifield, F.W.; Haines, P.J.; Oxford; Malden, MA : Blackwell Science, **2000,** 253-279
6. Wasinskim, Frank A.H.; Andersson, Jan T.; *J. Chromatogr. A*. **2007**, *1157*, 376-385
7. Heather, Rob, *GCQ: MS Detector Operator's and Service Manual,* Revision B, **1995**, 1.1
8. Chapman, J. R., *Practical Organic Mass Spectrometry: A Guide for Chemical and Biochemical Analysis,* 2nd, Chichester ; New York : John Wiley & Son, **c1993**.
9. Hewlett Packard, *Esquire-LC: Short Guide to Esquire-LC,* Version 3.1, **11/15/99**, 2.
10. Marotta, E.; Scorrano, G.; Paradisi, C.*; Rapid Commun. Mass Spectrom*. **2005**, 19, 1447-1453.

11. Brown, Michael E., *Introduction to Thermal Analysis: Techniques and Applications*, London, Chapman & Hall, **1988**.

12. Oswald, H.R.; Wiedemann, H.G.; *J. Thermal Anal*., **1977**, *12*, 147.

13. Taoana, T.L.N.; Holme, T.; Bariyanga, J.; *J. Mol. Struct*., **2004**, *694*, 173-178.

14. Fahmey, M.A.; Zayed, M.A.; El-Shobaky, H.G.; *J. Therm. Anal. Calorim*. **2005**, *82*, 137-142.

15. Corbi, Pedro P.; Massabni, Antonio C.; Costa-Neto, Claudio M.; *J. Coord. Chem*. **2005**, *Vol. 58*, No. 16. 1477-1483.

16. Zayed, M.A.; Fahmey, M.A.; Hawash, M.F.; Spectrochim. Acta, Part A, **2005**, *65*, 799-805.

17. Zayed, M.A.; El-shahat, M.F.; Abdullah, S.M.; Spectrochim. Acta, Part A, **2005**, *61*, 1955-1964.

18. Zayed, M.A.; Hawash, M.F.; Fahmey, M.A.; Spectrochim. Acta, Part A, **2006**, *64*, 363-371.

19. Zayed, M.A.; Hawash, M.F.; Fahmey, M.A.; El-Habeeb, Abeer A.; Spectrochim. Acta, Part A, **2007**, *68*, 970-978.

20. McLafferty, F.W.; *Interpretation of Mass Spectra*, 3rd, Mill Valley, California, University Science Books. **1980**

21. Hoffmann, Reinhard W.; *Synthesis*, **1982**, *2*, 107-109.

22. Runge, Franz; *Chemische Berichte*, **1954**, *V87*, 873-881.

23. Ecke, George G.; US 3075832, **1963.**

24. "International Chemical Safety Cards" data are provided by the National Library of Medicine (US).

Picture References

1. DSC schematics
   http://www.sv.vt.edu/classes/MSE2094_NoteBook/96ClassProj/experimental/dynamic/dynamic.html

Reversible Low Temperature Phase Change and Twinning in Lithium Acetyl Acetonate

Calvin A. Austin, Brian D. Leskiw, Matthias Zeller*

Youngstown State University, Department of Chemistry, 1 University Plaza, Youngstown Ohio 44555-3663, USA

Synopsis Lithium acetyl acetonate undergoes a reversible phase change from orthorhombic to non-merohedrally twinned monoclinic between 195 and 200 K. Differences between the structures are subtle and are basically limited to loss of perfect linearity of the $Li(acac)_n$ in the low temperature phase. Detailed descriptions of experimental procedures for the handling of non-merohedrally twinned datasets are given and discussed.

Abstract Lithium acetyl acetonate undergoes a perfectly reversible phase change from orthorhombic to non-merohedrally twinned monoclinic between 195 and 200 K. The phase transfer is associated with a sudden slight deviation of the orthorhombic γ-angle from 90°, with the initial coordinate changes following the phase transfer being very subtle. The connectivity within the lithium acetyl acetonate chains and the basic structural motif remain unchanged and the main difference between the orthorhombic and monoclinic structures is associated with a departure of the Li atoms - along with the Li(acac) chains as a whole - from a perfectly linear fashion in the room temperature structure to a slightly curved chain in the low temperature phase. Detailed descriptions of experimental procedures for the handling of non-merohedrally twinned datasets are given and discussed.

Keywords: [Click here to enter (separated by semicolons)]

1. Introduction and preliminary studies

Our interest into the structure of lithium acetyl acetonate initially arose from studies of two of us (BDL & CAA) on the ensuing gas phase reactions of a series of metal acetyl acetonate (acac) complexes. Through mass spectrometric analysis, several acetyl

acetonate and substituted acetyl aceonate species were observed to undergo various reactions including ligand insertion and exchange. Acetyl acetonates, and especially alkali metal acetyl acteonates, were also extensively studied as solids for their dielectric behaviour, and lithium acetyl acetonate has been used, among others, as an electron injection layers in some light emitting devices (Shi *et al.*, 2007). In this context Kamel *et al.* (1975) and Sawaand Abdel-Malik *et al.* (1992) also reported irreversible phase changes in both sodium and potassium acetyl acetonate from orthorhombic to triclinic upon heating above 353 and 313 K, respectively. The compounds studied by Kamel et al. and Abdel-Malik et al. were likely not sodium and potassium acetyl acetonate themselves (which still remain elusive), but their hydrates, as based on IR spectra (Molokhia & El-Shahat, 1981; Hemeda *et al.*, 1994).

Li(acac), on the other hand, is anhydrous, and its structure was initially reported independently by Schroeder & Weber and Onuma & Shibata in 1975 and 1978, respectively. Both structures were relatively inaccurate room temperature measurements with R values of 9.8 and 6.2%. For the purpose of having a reliable reference structure of this compound at hand for comparison with other acetyl acetonate complexes, we decided to recollect its data at lowered temperature. Being a supposedly straightforward and routine structure determination, the crystal at 100 K was, in fact, not C-centered orthorhombic, as reported previously, but non-merohedrally twinned in a primitive monoclinic setting with half the unit cell volume of the orthorhombic cell. The splitting of the diffraction spots was unambiguously obvious for reflections at relatively high angle, but using only low angle reflections allowed the dataset to be also tentatively indexed in the orthorhombic setting previously reported by Schroeder & Weber and Onuma & Shibata. In order to investigate whether this result was an indication of inaccuracies in the 30 year old literature reports, we re-collected the data at 293 K (using the same crystal). The results, however, verified that the structure at room temperature is indeed orthorhombic and C-centered.

2. Experimental

2.1. Sample preparation

The crystal used in the detailed studies that followed the initial discoveries was grown by slow evaporation of an ethanolic solution of commercially available Li(acac).

2.2. DSC measurements

Differential scanning calorimetric measurements were performed between -170 and 320 °C (103.5 and 493.5 K), thermal gravimetric analyses were performed between 20 and 590 °C (293.5 and 863.5 K) on both the Li(acac) samples as received as well as the samples recrystallized from ethanol. Up to 300 °C, no significant signals are observed during either the DSC or the TGA measurements (DSC and TGA plots are given in the supporting material). . No significant differential heat change was observed in the range of the phase transition between 180 and 220 K.

2.3. Powder XRD measurements

Powder X-ray diffraction measurements were performed at room temperature on a Bruker D8 Advance diffractometer using the Bragg-Brentano setup. Taking some preferential orientation of the samples into account, the measured spectra are in good agreement with data calculated from the single crystal datasets. Powder X-ray spectra are given in the supplementary material.

2.4. Single Crystal Data Collections

2.4.1. Experimental strategy

The data were collected on a Bruker AXS Smart Apex diffractometer equipped with a Kryoflex cooling system using monochromatic Mo Kα radiation with the omega scan technique. A clear and transparent plate, without any obvious breaks or discontinuities, was selected for the variable temperature studies and was mounted with help of a small amount of mineral oil onto a MiTeGen MicroMesh mount with 25 μm mesh size. The

crystal showed no visible signs of deterioration from the repeated heating and cooling experiments.

Full datasets were initially collected at 100 K and at room temperature (with the cooling unit switched off). Accurate unit cell determinations (with the crystal remaining mounted and centered all the time) were then collected at 100, 140, 160, 180, 185, 192, 194, 200, 205 and 220 K with 0.3° within frames and exposure times of 15 or 10 seconds per frame. For the datasets around the transition temperature (185, 192 and 194 K) full data collections were performed, for all others, 400 to 600 frames were collected at each temperature. After each temperature change the crystal was allowed to acclimatize to the new temperature for about 25-30 minutes. No recognizable delay time was detected for the crystal to adjust to each temperature

2.4.2. Data Processing and Refinement

Between 500 and 999 reflections were read in for each dataset using Smart (Bruker, 1997-2002), which was also used to determine the unit cells for the not twinned orthorhombic datasets. RLatt (Bruker, 2000) was used to inspect the collected reflections (the p4p files created) to initially distinguish non-merohedrally twinned structures from not twinned ones. Cell_Now (Sheldrick, 2005) was then used to determine the unit cells and orientation matrices of the twinned structures, the initial twin operations and the twin matrices. After full refinement of the first monoclinic dataset it became obvious that the monoclinic unit cells given by Cell_Now were in a non-standard setting in P2/n and they were thus converted into the conventional P2/c setting. Depending on the degree of overlap of the reflections of both components, a suitable deviation from the integer indices was chosen so that about two-thirds of the reflections were assigned to the first component identified. Using the new p4p file created by Cell_Now (containing the unit cell information and orientation matrices) Saint+ (Bruker, 2003) was used to integrate data with both one or two components, and to determine more accurate unit cell parameters and twin matrices. The s.u. values of the cell parameters are taken from the Saint+ software recognizing that the values are unreasonably small (Herbstein, 2000).

The 2007/3 release of Twinabs (Sheldrick 2007) was used to prepare both an hklf 4 and hklf 5 format file for the twinned datasets. The structure was solved by direct methods using the 100 K hklf 4 format file with only the non-overlapping reflections of one of the two components. In the hklf 5 format file, all reflections were merged according to point-group 2/m. Using the improved merging procedure in Version 2007/3 of Twinabs, single reflections that also occur in composites were omitted to avoid "twin pairing errors" (equivalent reflections being counted by Saint+ as overlapping for one reflection, but as not overlapping for an equivalent one, which would result in too many independent reflections and an indeterminable R_{int} value). The structures were then refined using this hklf 5 file with all reflections of component 1 (including the overlapping ones) below a d-spacing threshold of 0.75. The R_{int} values listed in the tables are based on all reflections as given in the output of Twinabs before the cutoff at d = 0.75. Untwinned data were corrected for absorption using Sadabs (Sheldrick 2007).

Using SHELXTL (Bruker 2000-2003) the structures were refined against F^2 using all reflections in the hkl files. Refinement of extinction coefficients was found to be insignificant. Non-hydrogen atoms were refined anisotropically. All hydrogen atoms were found in the difference density Fourier maps, but were ultimately added in calculated positions with C-H distances of 0.98 Å for methyl H atoms and 0.95 Å for the C-H bond, respectively, and were refined with $U_{iso}(H) = x\ U_{eq}(C)$ (x = 1.2 for C-H, 1.5 for CH_3). Methyl hydrogen atoms were allowed to rotate but not to tip to best fit the experimental electron density. Molecular diagrams were prepared using the graphical user interface of SHELXTL 6.14. (Bruker, 2000-2003).

3. Results and Discussion

3.1. Orthorhombic and Monoclinic Cells

The phase transition observed here is accompanied by a doubling of the unit-cell volume and a transition from the orthorhombic and C-centered room temperature setting to a non-

merohedrally twinned monoclinic and primitive setting. The monoclinic datasets could have been presented in either one of two equivalent settings in P2/n or P2/c related by the conversion matrix 1 0 0, 0 -1 0, -1 0 -1. The commonly accepted setting in P2/c was chosen over P2/n. Experimental details for each a representative monoclinic, orthorhombic and transitional dataset are given in Table 1.

No chemically significant differences are observed between the two structures, and the connectivity and general structural motif remains unchanged when passing through the phase transition. In contrast to its sodium and potassium analogues, the lithium acetyl acetonate is anhydrous in the solid state. It forms in both the monoclinic as well as the orthorhombic settings infinite chains of doubly μ-O bridged lithium atoms as previously described for the orthorhombic case by Schroeder & Weber (1975) and Onuma & Shibata (1978). Two chemically different types of Li cations are present: Lithium atoms roughly square planar coordinated by two acac anions, thus forming a monoanionic $Li(acac)_2^-$ subunit, and cations roughly tetrahedrally coordinated by four oxygen atoms from two $Li(acac)_2^-$ subunits. Figures 1a and 1b show the content of the asymmetric part of the unit cells of each the monoclinic and orthorhombic settings with the atom numbering scheme used; figures 2a and 2b depict packing diagrams for each of the two settings. In the orthorhombic setting the asymmetric part of the unit cell exhibits 1.5 molecules of Li(acac) with one acac ligand being located on one of the two fold axis parallel to the a-axis. Two of the four crystallographically independent lithium atoms (Li1 and Li4) are located on the intersection of all three two fold axes, and all four lithium atoms are located on the two fold axis paralleling the b-direction. The latter axis is also the direction of the infinite chain of lithium atoms. Each one of the cations that are located on the intersection of all three two fold axes is a square planar $Li(acac)_2^-$ type lithium atom (Li4), and the other, a tetrahedrally coordinated one (Li1). The Li atoms located only on one type of two fold axis – the axis parallel to b-direction – are also square planar and tetrahedral (Li2 and Li3), respectively

Upon transition into the monoclinic system the two fold axes (in the original orthorhombic setting) parallel to a and b along the Li chain are both lost and the

asymmetric part of the monoclinic cell now contains three Li(acac) units. Only one of the previously three types of glide planes is retained, and the sole remaining two fold axis is now aligned with the b-axis in the monoclinic setting (the c-axis in the orthorhombic setting and the viewing direction in Fig. 2a and 2b). Two of the four crystallographically independent lithium atoms are located on this remaining two fold axis. Each one of the cations still located on an axis is a square planar $Li(acac)_2^-$ type lithium atom (Li4), and the other a tetrahedrally coordinated one (Li1). The two Li atoms now located on general positions also belong to each one of the two types (square planar for Li2, tetrahedral for Li3).

The deviation of the atom positions from the orthorhombic setting right after the transition into the monoclinic phase is not very pronounced. Indeed, a check for missed symmetry using the Platon software (Spek, 2007) or Checkcif continues to indicate missed orthorhombic symmetry for temperatures down to nearly 180 K, close to 20 K below the transition temperature. The maximum deviation of the γ-angle (in the orthorhombic setting) at 194, 192 and 185 K, for example, is only 0.04, 0.59 and 0.78° respectively. Only at temperatures of less than 180 K does this angle finally reach a value deviating by more than one degree from that of the orthorhombic setting (the Platon threshold value for detection of missed symmetry). The atom positions at these temperatures, on the other hand, still differ only marginally from those in a hypothetical low temperature orthorhombic phase, the largest deviation for any atom at 194, 192 and 185K is 0.058, 0.070 and 0.141 Å respectively. Refinement of the 192 K dataset in the orthorhombic setting does indeed still give reasonably good results, with only marginally worse R values and structure quality indicators when compared to the refinement in the monoclinic setting (Table 1).

Upon further cooling the differences between the two structures become gradually more pronounced. When comparing the orthorhombic structure with that collected at 100 K, slight variations are increasingly apparent, with the most obvious one being a significant deviation of the lithium atoms from their previously orthorhombic symmetry imposed positions. Close inspection of the monoclinic structure reveal that the chains of lithium

atoms are now not arranged in a strictly linear fashion, but they start to be slightly offset - and with them the chains of Li(acac) as a whole - form a curved line instead of a straight chain as can be seen in Fig 2a. A closer analysis (Fig 3) reveals that all Li atoms deviate somehow from the ideal linear chain present in the orthorhombic structure. For Li2 and Li3 the deviations are mainly in the direction of both the monoclinic b- and c-axes. Li1 and Li4, which are located to the two fold axis parallel to b, are displaced only along the c-axis (Fig 3).

3.2. Diffraction Patterns

With the actual structural changes between the orthorhombic and twinned monoclinic phases being rather small, the most reliable method to verify the actual presence of a phase transition and to determine its nature and transition temperature is examination of the diffraction patterns - especially when the phase change is associated with the emergence of non-merohedral twinning. Fig. 3 shows three screenshots of frames recorded at 180, 190 and 198 K with the crystal in a random but identical orientation (additional screenshots at other temperatures and orientations are provided in the supporting material). On each frame several sets of diffraction spots undergoing transition from monoclinic twinned to orthorhombic are immediately visible in the lower half of the diffraction pattern screenshots. At 180 K, well below the transition temperature, several reflections are clearly split with one reflection of each pair belonging to one component of the twin and the other to the second. At 190 K, just below the transition temperature, the pairs begin to merge, and at 198 K this process is completed and all diffraction spots are unambiguously single and unique, with the structure now being orthorhombic.

3.3. Unit cell parameters

Unit cell parameters at a series of temperatures around the transition temperature, ranging from 100 to 220 K, are given in Table 2. Determination of accurate unit cell parameters for non-merohedrally twinned data sets remains a challenge despite continuous improvement in software and the large number of reflections available with area detector data. Unit cell determination close to the transition temperature is especially challenging

given the associated uncertainties and the data have to be used with great caution. With the exception of the γ-angle (the angle that becomes different from 90 degrees in the orthorhombic setting upon cooling below the transition temperature) all observed unit cell parameter values show only small changes with change in temperature, and no obvious trend for these can be deduced from the data. The γ-angle, however, drastically drops from the ideal value of 90° upon cooling to the transition temperature, and then gradually approaches a new value of about 88.25° when cooling further down to about 100 K. It seems that a certain amount of strain is building up within the orthorhombic structure just above the transition temperature. Upon actually reaching the transition point, this strain is suddenly released with a rather large immediate change, followed by a more gradual adjustment of the angle to reach the new angle found in the monoclinic cells.

4. Summary

The above observations - a sudden change of the γ-angle in combination with the loss of linearity of the Li(acac) chains - point towards an intricate interplay of enthalpy and entropy as the driving force behind the phase transition. The nonlinear chains in the monoclinic structure - as the enthalpically more stable phase - are the thermodynamically favoured motif. At lower temperature the interactions of the chains with their individual neighbours are sufficient to enforce long range order throughout large domains of the crystal thus imposing the monoclinic structure on each of these domains. The interactions are, on the other hand, not sufficient to impede occasional defects where neighbouring domains may have opposing twin orientations. Upon reaching the transition temperature the thermal movement of the atoms reaches a threshold and the interactions of neighbouring chains is not sufficient enough any more to maintain long range order. Without effective lateral transfer of information between the chains, the positions of the Li(acac) chains become random with respect to deviation from the chain axis and average out to zero for the crystal as a whole. The structure is now orthorhombic.

5. Supporting Material

TGA and DSC plots for recrystallized and as purchased lithium acteylacetonate; powder X-ray diffractogram and fit to simulated orthorhombic structure; cif files, structure factors and Checkcif reports for datasets collected at 100 K, 192 K (both refined as orthorhombic and monoclinic) and room temperature; Platon Missym results for datasets collected at 185, 192 and 194K; and more frame screenshots (each 12 for two different crystal orientations between 100 K and 200 K).

Figure 1 Asymmetric units with atom numbering scheme for (a) the monoclinic twinned structure (at 100 K), (b) the orthorhombic structure (at 298 K)

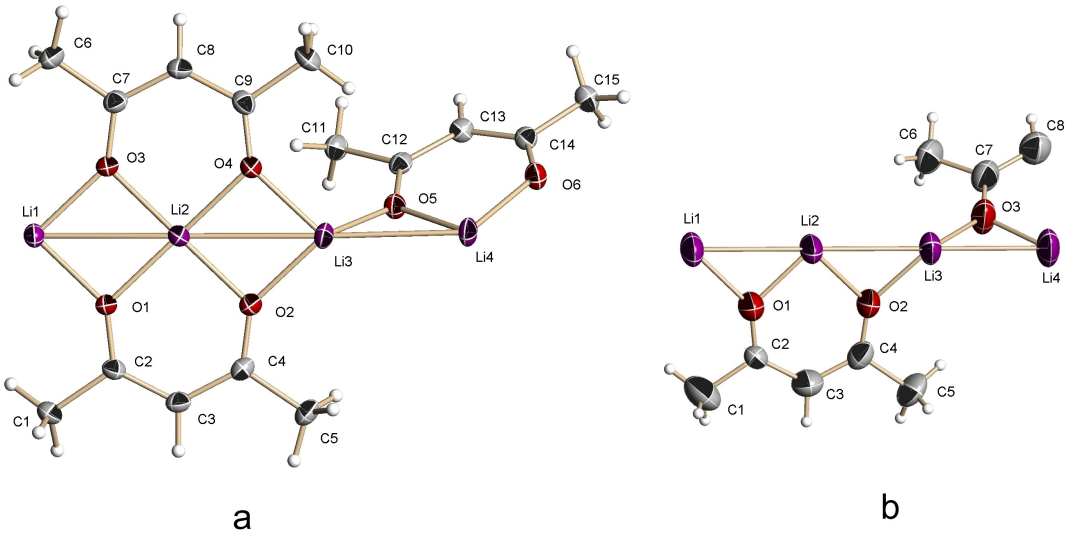

Figure 2 Packing views of (a) the monoclinic twinned structure (at 100 K), (b) the orthorhombic structure (at 298 K). The viewing direction is along the two fold axis in the monoclinic setting (b-axis) and the equivalent direction of the orthorhombic cell (c-axis), respectively. Note the not quite linear (wavy) Li-chains in the monoclinic setting in (a) vs the Li atoms being located on a two fold axis parallel to the orthorhombic b-axis in (b).

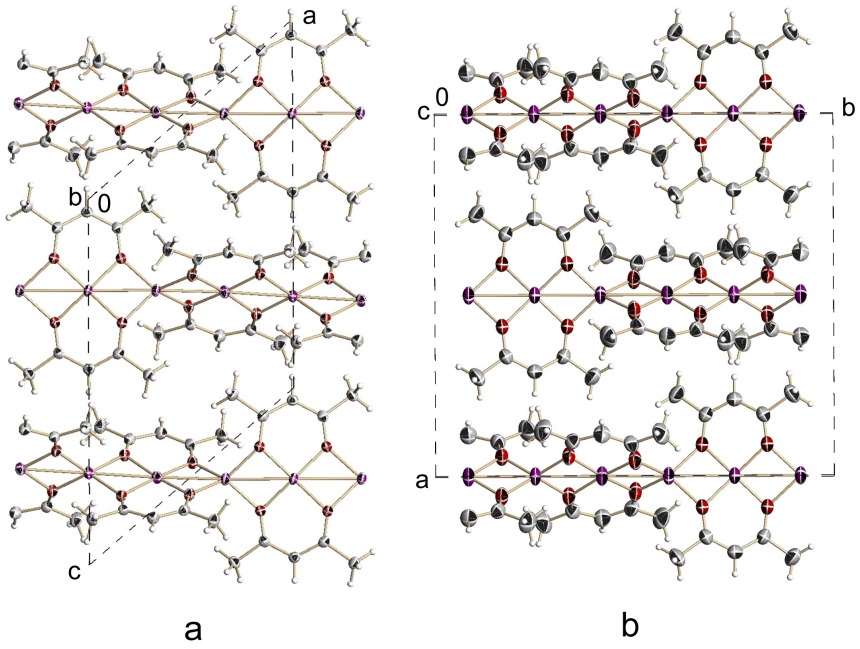

Figure 3 Deviation of the lithium atoms at 100 K from an ideal linear chain (based on symmetry restraints in a hypothetical orthorhombic structure).

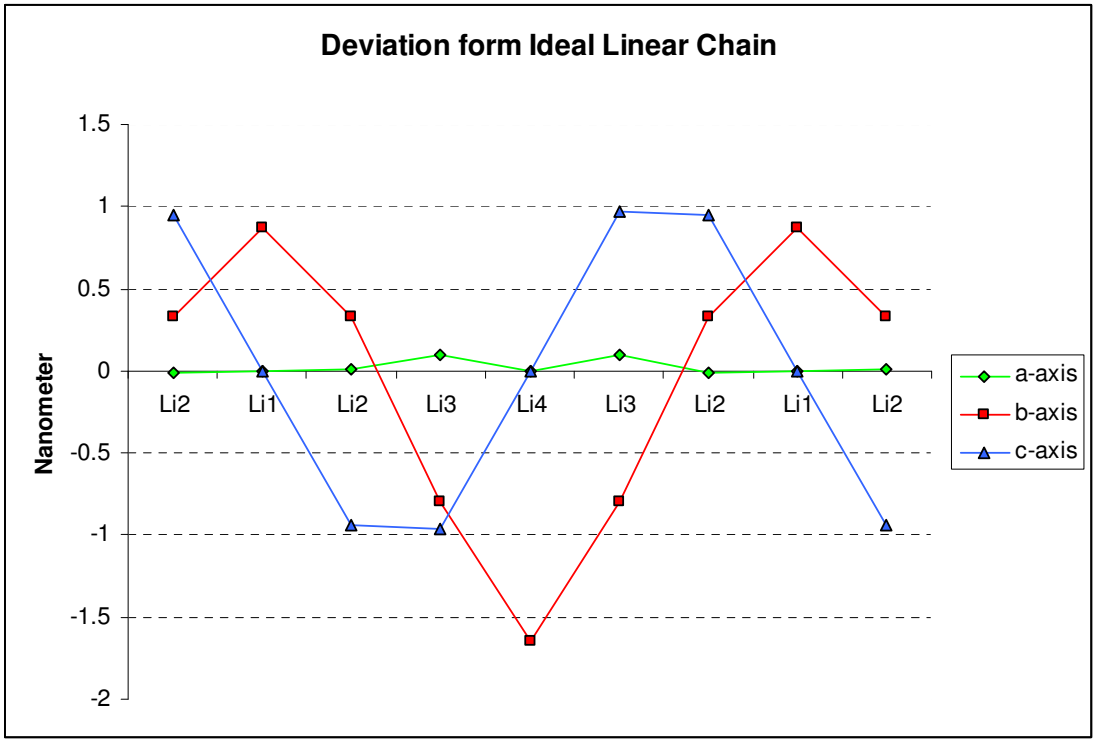

Figure 4 Typical diffraction patterns of Li(acac) around the transition point at 180, 190, and 198 K.

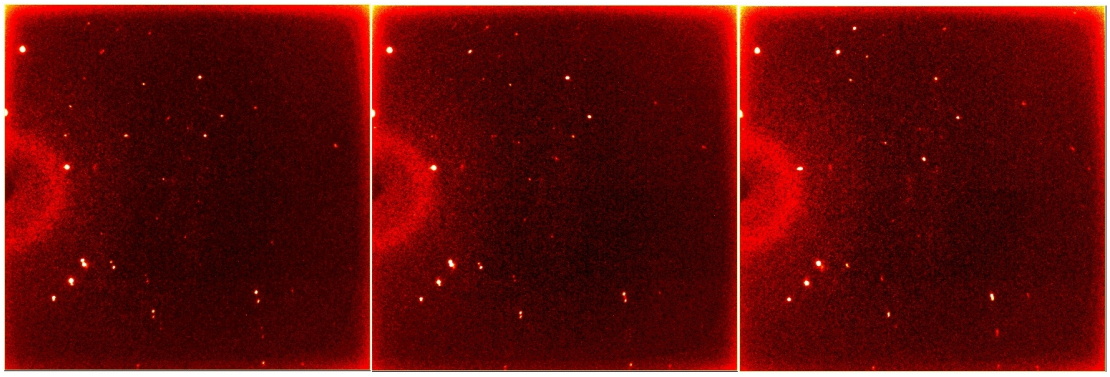

Figure 5 Plot of the γ-angle in the orthorhombic setting against the measurement temperature. Data collected up to 194 K are converted from the twinned monoclinic setting by application of the transformation matrix 0 0 -1, -2 0 -1, 0 1 0.

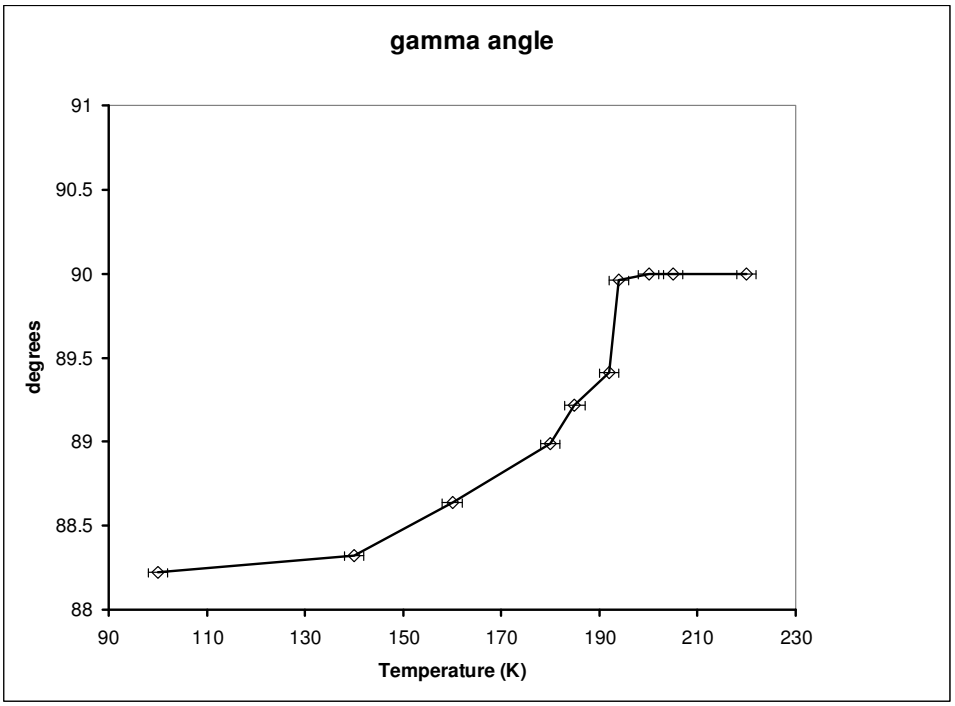

Table 1 Experimental details for three representative datasets collected at 100 K (monoclinic twinned, below the transition temperature) and at 298 K (orthorhombic,

above the transition), and 192 K (just below the transition temperature refined in both alternative settings).

Formula	$C_{15}H_{21}Li_3O_6$	$C_{15}H_{21}Li_3O_6$	$C_{7.5}H_{10.5}Li_{1.5}O_3$	$C_{7.5}H_{10.5}Li_{1.5}O_3$
Moiety formula	3 ($C_5H_7LiO_2$)	3 ($C_5H_7LiO_2$)	1.5 ($C_5H_7LiO_2$)	1.5 ($C_5H_7LiO_2$)
Formula weight	318.14	318.14	106.05	106.05
Temperature	100(2) K	192(2) K	192(2) K	298(2) K
Wavelength	0.71073 Å	0.71073 Å	0.71073 Å	0.71073 Å
Crystal system	Monoclinic	Monoclinic	Orthorhombic	Orthorhombic
Space group	P2/c	P2/c	Ccca	Ccca
Unit cell dimensions	a = 11.0770(13) b = 13.6854(16) c = 14.9649(17) β = 130.648(2)	a = 11.264(3) b = 13.839(4) c = 15.109(5) β = 131.525(6)	a = 15.0954(16) b = 16.8256(18) c = 13.8290(15)	a = 15.2138(12) b = 16.7859(13) c = 13.9889(12)
Volume, Z	1721.2(3), 4	1763.3(9), 4	3512.4(7), 24	3572.4(5), 24
Density (calculated)	1.228	1.198	1.203	1.183
Absorption coefficient	0.090	0.088	0.088	0.087
F(000)	672	672	1344	1344
Crystal size	0.38 × 0.37 × 0.17 mm^3	0.38 × 0.37 × 0.17 mm^3	0.38 × 0.37 × 0.17 mm^3	0.38 × 0.37 × 0.17 mm^3
Crystal shape, colour	Plate, colourless	Plate, colourless	Plate, colourless	Plate, colourless
θ range for data collection	1.49-28.28	1.47-28.28	2.34-28.28	2.32-28.28

Limiting indices	$-14 \le h \le 11$ $0 \le k \le 18$ $0 \le l \le 19$	$-15 \le h \le 11$ $0 \le k \le 18$ $0 \le l \le 20$	$-20 \le h \le 20$ $-19 \le k \le 22$ $-18 \le l \le 18$	$-20 \le h \le 17$ $-18 \le k \le 22$ $-14 \le l \le 18$
Reflections collected	31996 (8802 twin overlaps)	19970 (18126 twin overlaps)	14597	9422
Independent reflections	4282	4375	2181	2224
Completeness to $\theta = 28.28°$	100.0 %	99.9 %	99.8 %	100.0 %
Absorption correction	Multi-scan	Multi-scan	Multi-scan	Multi-scan
Max. and min. transmission	0.845 and 0.985	0.871 and 0.985	0.819 and 0.862	0.819 and 0.985
Refinement method	Full-matrix least-squares on F^2	Full-matrix least-squares on F^2	Full-matrix least-squares on F^2	Full-matrix least-squares on F^2
Data / restraints / parameters	4282 / 0 / 225	4375 / 0 / 225	2181 / 0 / 115	2224 / 0 / 115
Goodness-of-fit	1.045	1.059	1.107	1.045
Final R indices [I>2σ(I)]	R1 = 0.0616, wR2 = 0.1670	R1 = 0.0533, wR2 = 0.1193	R1 = 0.0576, wR2 = 0.1743	R1 = 0.0606, wR2 = 0.1766
R indices (all data)	R1 = 0.0762, wR2 = 0.1870	R1 = 0.0856, wR2 = 0.1413	R1 = 0.0732, wR2 = 0.1865	R1 = 0.0808, wR2 = 0.1991
Twinning ratio	0.423(2)	0.480(5)	-	-
Largest diff. hole and peak	-0.290 and 0.567 e × Å^{-3}	-0.193 and 0.260 e × Å^{-3}	-0.246 and 0.272 e × Å^{-3}	-0.160 and 0.369 e × Å^{-3}

Table 2 Unit cell parameters of Li(acac) in the "orthorhombic setting" between 100 and 220 K. Data sets collected up to 194 K are converted from the twinned monoclinic setting.

Collection Temp. [K]	a-axis	b-axis	c-axis	α-angle	β-angle	γ-angle	volume
100	14.972	16.816	13.711	90	90	88.22	3450
140	14.998	16.835	13.733	90	90	88.32	3465
160	15.009	16.816	13.764	90	90	88.64	3473
180	15.009	16.799	13.742	90	90	88.99	3464
185	15.024	16.806	13.780	90	90	89.22	3479
192	15.109	16.867	13.939	90	90	89.41	3511
194	15.078	16.814	13.821	90	90	89.96	3496
200	15.119	16.833	13.846	90	90	90	3524
205	15.127	16.831	13.854	90	90	90	3527
220	15.093	16.810	13.833	90	90	90	3510

Acknowledgements The authors would like to thank Michael Ruf and Susan Byram of Bruker AXS for providing a copy of twinabs version 2007/3 prior to its official release. The diffractometer was funded by NSF grant 0087210, by Ohio Board of Regents grant CAP-491, and by YSU.

References

Abdel-Malik, T. G., Kassem, M. E., Abdel-Latif, R. M., & Khalil, S. M. (1992). Acta Physica Polonica A, 81(6), 681-686.

Bruker (1997-2002). SMART for WNT/2000 5.630. Bruker AXS Inc, Madison (WI), USA.

Bruker (2003). SAINT+ 6.45. Bruker AXS Inc, Madison (WI), USA.

Bruker (2000-2003). SHELXTL 6.14. Bruker AXS Inc, Madison (WI), USA.

Bruker (2000). RLatt, Reciprocal Lattice Viewer version 3.0, Bruker AXS Inc, Madison (WI), USA.

Hemeda, O. M., Ayad, M. I, Henaish, M. A., & Abou Sekkina, M. M. (1994). Phase Transitions, 48, 207-215.

Herbstein, F. H. (2000). Acta Cryst. B56, 547-557.

Kamel, R., Hilal, M., Eid, A. H., & Sawaby, A. (1975). Mol. Cryst. Liq. Cryst., 31, 9-19.

Molokhia, N. M, & El-Shahat, M. F. (1981). J. Chem. Tech. Biotechol., 31, 619-623.

Onuma, S., Shibata, S. (1978). Reports of Faculty of Science, Shizuoka University, 12, 45-56.

Schroeder, F. A.; Weber, H. P. (1975). Acta Cryst B, 31(6), 1745-50.

Sheldrick, G. M. (2007). Twinabs, Bruker AXS scaling for twinned crystals, version 2007/3, & Sadabs, Bruker AXS area detector scaling and absorption correction, version 2007/2,University of Göttingen, Germany & Bruker AXS Inc, Madison (WI), USA.

Shi, S., Ma, D., & Peng, J. (2007). Semicond. Sci. Technol., 22, 249-252.

Spek, A. L. (2007). Platon, A Multipurpose Crystallographic Tool, 40M-Version: 40607, 1980-2007.

Sheldrick, G. M. (2005). CELL NOW, program for unit cell determination, University of Göttingen, Germany & Bruker AXS Inc, Madison (WI), USA.